

# LDLE: Low Distortion Local Eigenmaps

Dhruv Kohli<sup>a,\*</sup>, Alexander Cloninger<sup>a,b</sup>, Gal Mishne<sup>b</sup>

<sup>a</sup>*Department of Mathematics, University of California, San Diego, CA*

<sup>b</sup>*Halicioğlu Data Science Institute, University of California, San Diego, CA*

---

## Abstract

We present Low Distortion Local Eigenmaps (LDLE), a manifold learning technique which constructs a set of low distortion local views of a dataset in lower dimension and registers them to obtain a global embedding. The local views are constructed using the global eigenvectors of the graph Laplacian and are registered using Procrustes analysis. The choice of these eigenvectors may vary across the regions. In contrast to existing techniques, LDLE is more geometric and can embed manifolds without boundary as well as non-orientable manifolds into their intrinsic dimension.

*Keywords:* Manifold learning, graph Laplacian, local correlation, Procrustes analysis, low distortion, no boundary, non-orientable.

---

## 1. Introduction

Nonlinear dimensionality reduction techniques such as Local Linear Embedding [1], Hessian eigenmaps [2], Laplacian eigenmaps [3], t-SNE [4] and UMAP [5], aim at preserving local distances as they map a manifold embedded in higher dimension into lower (possibly intrinsic) dimension. In particular, UMAP and t-SNE follow a top-down approach where they start with an initial low-dimensional global embedding and then refine it by minimizing a local distortion measure on it. In contrast, a bottom-up embedding approach can be imagined to consist of two steps, first obtaining low distortion local views of the manifold in lower dimension and then registering them to obtain a global embedding of the manifold. These local views can be constructed using the coordinate charts of the manifold. For this paper, we take the local perspective to embed a manifold in low dimension.

Let  $(\mathcal{M}, g)$  be a  $d$ -dimensional Riemannian manifold with finite volume. By definition, for every  $x_k$  in  $\mathcal{M}$ , there exists a coordinate chart  $(\mathcal{U}_k, \Phi_k)$  such that  $x_k \in \mathcal{U}_k$ ,  $\mathcal{U}_k \subset \mathcal{M}$  and  $\Phi_k$  maps  $\mathcal{U}_k$  into  $\mathbb{R}^d$ . One can imagine  $\mathcal{U}_k$  to be a local view of  $\mathcal{M}$  in the ambient space. Using rigid transformations, these local views can be registered to recover  $\mathcal{M}$ . Similarly,  $\Phi_k(\mathcal{U}_k)$  can be imagined to be a local view of  $\mathcal{M}$  in the  $d$ -dimensional embedding space  $\mathbb{R}^d$ . Again using rigid transformations, these local views can be registered to obtain the  $d$ -dimensional embedding of  $\mathcal{M}$ .

As there may exist multiple mappings which map  $\mathcal{U}_k$  into  $\mathbb{R}^d$ , a natural strategy would be to choose a mapping with low distortion. This would result in an embedding in which the local geodesic distances are approximately preserved. Let  $d_g(x, y)$  denote the shortest geodesic distance between  $x, y \in \mathcal{M}$ . The distortion of  $\Phi_k$  on  $\mathcal{U}_k$  as defined in [6] is given by

$$\text{Distortion}(\Phi_k, \mathcal{U}_k) = \|\Phi_k\|_{Lip} \|\Phi_k^{-1}\|_{Lip} \quad (1)$$

---

\*Corresponding author

*Email addresses:* [dhkohli@ucsd.edu](mailto:dhkohli@ucsd.edu) (Dhruv Kohli), [acloninger@ucsd.edu](mailto:acloninger@ucsd.edu) (Alexander Cloninger), [gmishne@ucsd.edu](mailto:gmishne@ucsd.edu) (Gal Mishne)

where  $\|\Phi_k\|_{Lip}$  is the Lipschitz norm of  $\Phi_k$  given by

$$\|\Phi_k\|_{Lip} = \sup_{\substack{x,y \in \mathcal{U}_k \\ x \neq y}} \frac{\|\Phi_k(x) - \Phi_k(y)\|_2}{d_g(x,y)}, \quad (2)$$

and similarly,

$$\|\Phi_k^{-1}\|_{Lip} = \sup_{\substack{x,y \in \mathcal{U}_k \\ x \neq y}} \frac{d_g(x,y)}{\|\Phi_k(x) - \Phi_k(y)\|_2}. \quad (3)$$

If  $\text{Distortion}(\Phi_k, \mathcal{U}_k) = 1$ , then  $\Phi_k$  is said to have no distortion on  $\mathcal{U}_k$ . It is not always possible to obtain a mapping with no distortion. For example, a locally curved region on a surface cannot be isometrically mapped into a Euclidean plane.

### 1.1. Related Work

Various algorithms for manifold learning including Laplacian eigenmaps [3], UMAP [5], and t-SNE [4] also focus on preserving local distances. Laplacian eigenmaps uses the eigenvectors corresponding to the  $d$  smallest eigenvalues (excluding zero) of the normalized graph Laplacian to embed the manifold in  $\mathbb{R}^d$ . For manifolds with high aspect ratio, the distortion of the local parameterizations based on these eigenvectors could become extremely high. For example, as shown in Figure 1, the Laplacian eigenmaps embedding of a rectangle with an aspect ratio of 16 looks like a parabola. To a large extent UMAP resolves this issue by first computing an embedding by applying standard spectral methods on a symmetric normalized Laplacian and then “sprinkling” white noise in it. It then refines the noisy embedding by minimizing a local distortion measure based on fuzzy set cross entropy. Although UMAP embeddings seem to be topologically correct, they occasionally tend to have twists and sharp turns which may be unwanted (see Figure 1). t-SNE takes a different approach of randomly initializing the global embedding, defining a local t-distribution in the embedding space and local Gaussian distribution on the high dimensional points, and finally refining the embedding by minimizing the Kullback–Leibler divergence between the two sets of distributions. As shown in Figure 1, t-SNE tends to output a dissected embedding even when the manifold is connected.

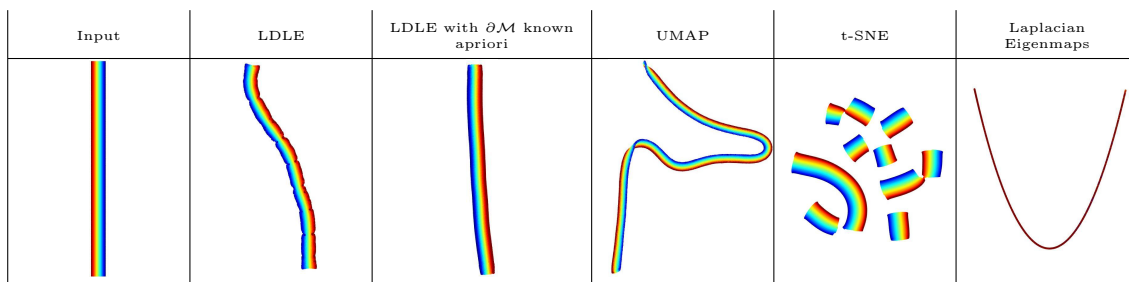


Figure 1: Embeddings of a rectangle ( $4 \times 0.25$ ) with high aspect ratio in  $\mathbb{R}^2$  into  $\mathbb{R}^2$ .

Another missing feature in the above methods is their ability to embed manifolds without boundary into their intrinsic dimensions. For example, a sphere in  $\mathbb{R}^3$  is a 2-dimensional manifold which can be represented by a connected domain in  $\mathbb{R}^2$  with boundary gluing instructions provided in the form of colors. We solve this issue in this paper (see Figure 2).

This paper takes motivation from the work of Jones, Maggioni, and Schul in [6] where they provide guarantees on the distortion of the coordinate charts of the manifold constructed using carefully chosen eigenfunctions of the Laplacian. However, this only applies to the charts for small neighborhoods on the manifold and

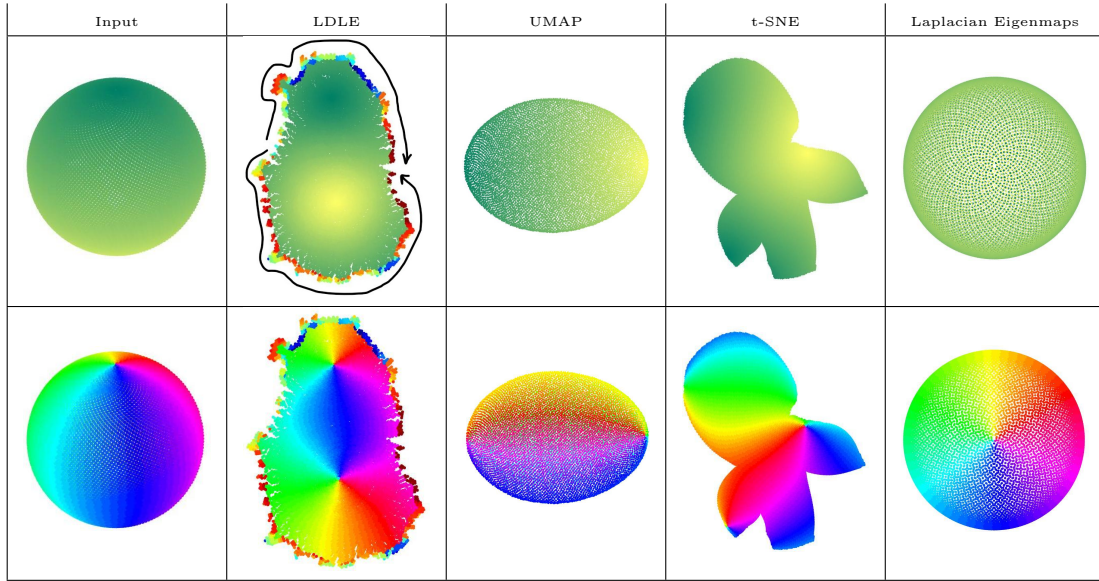


Figure 2: Embeddings of a sphere in  $\mathbb{R}^3$  into  $\mathbb{R}^2$ . The top and bottom row contain the same plots colored by the height and the azimuthal angle of the sphere ( $0 - 2\pi$ ), respectively. LDLE automatically colors the boundary so that the points on the boundary which are adjacent on the sphere have the same color. The arrows are manually drawn to help the reader identify the two pieces of the boundary which are to be stitched together to recover the original sphere. UMAP and Laplacian eigenmaps squeezed the sphere into two different viewpoints of  $\mathbb{R}^2$  (side or top view of the sphere). t-SNE also tore apart the sphere but the embedding lacks interpretability as it is “unaware” of the boundary.

does not provide a global embedding. In this paper, we present an approach to realize their work in the discrete setting and obtain low-dimensional low distortion local views of the given dataset. Moreover, we piece together these local views to obtain a global embedding of the manifold.

### 1.2. Our Contributions

In this paper we present Low Distortion Local Eigenmaps (LDLE), a new manifold learning approach. The main contributions of our work are as follows:

1. We present an algorithmic realization of the construction procedure in [6] that applies to the discretized setting and yields low-dimensional low distortion views of small metric balls on the given discretized manifold (See Section 2 for a summary of their procedure).
2. We present an algorithm to obtain a global embedding of the manifold by registering its local views. The algorithm is designed so as to embed manifolds without boundary as well as non-orientable manifolds into their intrinsic dimension by tearing them apart. It also provides gluing instructions for the boundary of the embedding by coloring it such that the points on the boundary which are adjacent on the manifold have the same color (see Figure 2).

LDLE consists of three main steps. In the first step, we estimate the inner product of the eigenfunctions using the local correlation between them to construct low-dimensional low distortion parameterizations  $\Phi_k$  of the small discrete balls  $U_k$  on the discretized manifold. In the second step, we develop a clustering algorithm to obtain a small number of intermediate views  $\tilde{\Phi}_m(\tilde{U}_m)$  with low distortion, from the large number of smaller local views  $\Phi_k(U_k)$ . This makes the subsequent registration procedure faster and less prone to errors. Finally, in the third step, we register the intermediate views  $\tilde{\Phi}_m(\tilde{U}_m)$  and obtain the final global embedding of  $\mathcal{M}$ . The results on a 2D rectangular strip and a 3D sphere are presented in Figures 1 and 2, to motivate our approach.

The paper organization is as follows. Section 2 provides relevant background and motivation. In section 3 we present the construction of low-dimensional low distortion local parameterizations. Section 4 presents our clustering algorithm to obtain intermediate views. Section 5 registers the intermediate views to a global embedding. In section 6 we compare the embeddings produced by our algorithm with existing techniques on multiple datasets. Section 7 concludes our work and discusses directions for future work.

## 2. Background and Motivation

Manifold learning techniques such as Laplacian eigenmaps [3], Diffusion maps [11] and UMAP [5] rely on a fixed set of eigenfunctions of the Laplacian operator to construct a low-dimensional embedding of the manifold. The following example illustrates that a mapping based on a fixed set of eigenfunctions may not provide low distortion on different  $\mathcal{U}_k$  and  $\mathcal{U}_{k'}$ . This is why a postprocessing step such as in UMAP, that minimizes a local distortion measure on the embedding becomes necessary when using the above techniques to obtain a low distortion embedding of the manifold.

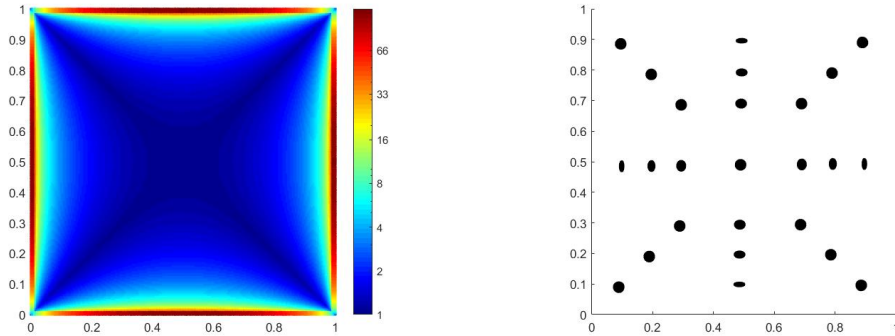


Figure 3: (Left) Distortion of  $\Phi_1^*$  on discs of radius 0.01 centered at  $(x, y)$  for all  $x, y \in [0, 1] \times [0, 1]$ . (Right) Mapping of the discs at various locations in the square using  $\Phi_1^*$ .

Consider a unit square  $[0, 1] \times [0, 1]$  such that for every point  $x_k$  in the square,  $\mathcal{U}_k$  is the disc of radius 0.01 centered at  $x_k$ . Consider a mapping  $\Phi_1^*$  based on the first two non-trivial eigenfunctions  $\cos(\pi x)$  and  $\cos(\pi y)$  of the Laplace-Beltrami operator on the square with Neumann boundary conditions, that is,

$$\Phi_1^*(x, y) = (\cos(\pi x), \cos(\pi y)). \quad (4)$$

As shown in Figure 3,  $\Phi_1^*$  maps the discs along the diagonals to other discs. The discs along the horizontal and vertical lines through the center are mapped to ellipses. The skewness of these ellipses increases as we move closer to the middle of the edges of the unit square. Thus, the distortion of  $\Phi_1^*$  is low on the discs along the diagonals and high on the discs close to the middle of the edges of the square.

Now, consider a different mapping based on another set of eigenfunctions,

$$\Phi_2^*(x, y) = (\cos(5\pi x), \cos(5\pi y)). \quad (5)$$

Compared to  $\Phi_1^*$ ,  $\Phi_2^*$  produces almost no distortion on the discs of radius 0.01 centered at  $(0.1, 0.5)$  and  $(0.9, 0.5)$  (see Figure 4). Therefore, it makes sense to construct local mappings for different regions based on different sets of eigenfunctions to obtain their embeddings with low distortion.

At this point we state a result from [6] which shows the existence of low distortion parameterizations of small metric balls on a Riemannian manifold of finite volume using the globally defined eigenfunctions of the Laplacian. The choice of the eigenfunctions depend on the underlying metric ball.

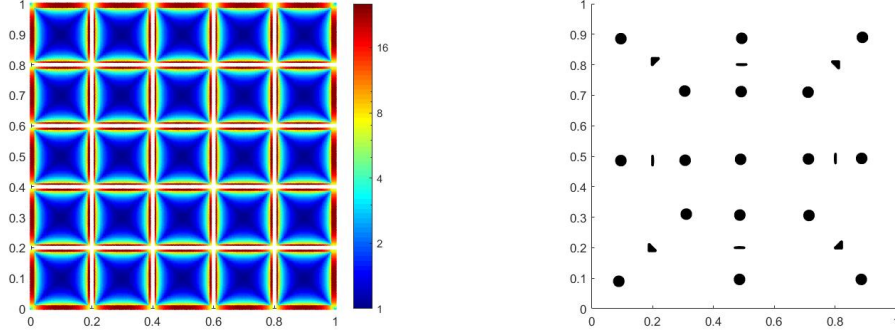


Figure 4: (Left) Distortion of  $\Phi_2^*$  on discs of radius 0.01 centered at  $(x, y)$  for all  $x, y \in [0, 1] \times [0, 1]$ .  $\Phi_2^*$  produces close to infinite distortion on the discs located in the white region. (Right) Mapping of the discs at the same locations in the square as in Figure 3 using  $\Phi_2^*$ .

**Theorem 1** (see Theorem 2.2.1 in [6]). *Let  $(\mathcal{M}, g)$  be a  $d$ -dimensional Riemannian manifold. Let  $\Delta_g$  be the Laplace-Beltrami operator on it with Dirichlet or Neumann boundary conditions. Assume that  $|\mathcal{M}| = 1$  where  $|\mathcal{M}|$  is the volume of  $\mathcal{M}$  and the uniform ellipticity conditions for  $\Delta_g$  are satisfied. Let  $x_k \in \mathcal{M}$  and  $r_k$  be less than the injectivity radius at  $x_k$  (the maximum radius where the exponential map is a diffeomorphism). Then, there exists a constant  $\kappa > 1$  which depends on  $d$  and the metric tensor  $g$  such that the following hold. Let  $\rho \leq r_k$  and  $B_k \equiv B_{\kappa^{-1}\rho}(x_k)$  where*

$$B_\epsilon(x) = \{y \in \mathcal{M} \mid d_g(x, y) < \epsilon\}. \quad (6)$$

Then there exist  $i_1, i_2, \dots, i_d$  such that, if we let

$$\gamma_{ki} = \left( \frac{\int_{B_k} \phi_i^2(y) dy}{|B_k|} \right)^{-1/2} \quad (7)$$

then the map

$$\begin{aligned} \Phi_k : B_k &\rightarrow \mathbb{R}^d \\ x &\rightarrow (\gamma_{ki_1} \phi_{i_1}(x), \dots, \gamma_{ki_d} \phi_{i_d}(x)) \end{aligned} \quad (8)$$

is bilipschitz such that for any  $y_1, y_2 \in B_k$  it satisfies

$$\frac{\kappa^{-1}}{\rho} d_g(y_1, y_2) \leq \|\Phi_k(y_1) - \Phi_k(y_2)\| \leq \frac{\kappa}{\rho} d_g(y_1, y_2), \quad (9)$$

where the associated eigenvalues satisfy

$$\kappa^{-1} \rho^{-2} \leq \lambda_{i_1}, \dots, \lambda_{i_d} \leq \kappa \rho^{-2}, \quad (10)$$

and the distortion is bounded from above by  $\kappa^2$  i.e.

$$\sup_{\substack{y_1, y_2 \in B_k \\ y_1 \neq y_2}} \frac{\|\Phi_k(y_1) - \Phi_k(y_2)\|}{d_g(y_1, y_2)} \sup_{\substack{y_1, y_2 \in B_k \\ y_1 \neq y_2}} \frac{d_g(y_1, y_2)}{\|\Phi_k(y_1) - \Phi_k(y_2)\|} \leq \frac{\kappa}{\rho} \frac{\rho}{\kappa^{-1}} = \kappa^2. \quad (11)$$

*Construction Procedure.* In [6] the authors describe a procedure to choose the eigenfunctions for  $\Phi_k$  as summarized below. The main aim is to identify  $d$  eigenfunctions such that they are close to being locally orthogonal and that their local scaling factors  $\gamma_{ki_s} \|\nabla \phi_{i_s}(x_k)\|_2$  are close to each other.

Under the assumptions of the theorem, the authors showed that, for all  $i$ ,  $\gamma_{ki} \|\nabla\phi_i(x_k)\|_2$  is bounded from above where the bound depends on  $\lambda_i\rho^2$ . Therefore, any choice of the eigenfunctions would result in a Lipschitz map. However, satisfying the Lipschitz condition alone is not sufficient to obtain low distortion. For example, a  $\Phi_k$  which maps  $B_k$  to a fixed point is trivially Lipschitz but has infinite distortion. It is necessary for  $\Phi_k$  to satisfy the bilipschitz condition to at least ensure finite distortion. Since  $\gamma_{ki} \|\nabla\phi_i(x_k)\|_2$  is already bounded from above, the bilipschitz condition for  $\Phi_k$  can be satisfied by choosing the eigenfunctions for which  $\gamma_{ki} \|\nabla\phi_i(x_k)\|_2$  is also bounded from below. Although this would result in  $\Phi_k$  having finite distortion on  $B_k$ , one cannot guarantee it to be low. Suppose  $\phi_{i_1}$  and  $\phi_{i_2}$  satisfy the above condition, two scenarios are possible which can lead to high distortion:

1. If the vectors  $\nabla\phi_{i_1}(x_k)$  and  $\nabla\phi_{i_2}(x_k)$  are far from being orthogonal then  $\Phi_k$  would squeeze the first two dimensions of  $B_k$  into a single dimension.
2. If the local scaling factors  $\gamma_{ki_1} \|\nabla\phi_{i_1}(x_k)\|_2$  and  $\gamma_{ki_2} \|\nabla\phi_{i_2}(x_k)\|_2$  are far from each other then  $\Phi_k$  would result in a highly skewed output along the two dimensions.

Thus, to obtain low distortion, the authors proposed the following procedure to select the eigenfunctions so that  $\Phi_k$  is bilipschitz and avoids the above scenarios as much as possible.

First, a subset  $S_k$  of the eigenfunctions is chosen such that for all  $i \in S_k$ ,  $\lambda_i\rho^2$  is bounded within a specific interval. This interval eventually comes out to be  $[\kappa^{-1}, \kappa]$  (see Eq. (10)). Then, a direction  $p_1$  is selected at random and subsequently  $i_1 \in S_k$  is selected so that  $\gamma_{ki_1} |\nabla\phi_{i_1}(x_k)^T p_1|$  is larger than  $c_0\rho^{-1}$  where  $c_0$  depends on the geometric properties of  $\mathcal{M}$ . Then, to find the  $s$ -th eigenfunction for  $s \in \{2, \dots, d\}$ , a direction  $p_s$  is chosen such that it is orthogonal to  $\nabla\phi_{i_1}(x_k), \dots, \nabla\phi_{i_{s-1}}(x_k)$ . Subsequently,  $i_s \in S_k$  is chosen so that  $\gamma_{ki_s} |\nabla\phi_{i_s}(x_k)^T p_s|$  is again larger than  $c_0\rho^{-1}$ . The core of their work lies in proving that these  $i_1, \dots, i_d$  always exist under the assumptions of the theorem.

It is easy to discern that the above procedure motivates the chosen eigenfunctions to be locally orthogonal. The requirement of  $\gamma_{ki_s} |\nabla\phi_{i_s}(x_k)^T p_s|$  to be larger than  $c_0\rho^{-1}$  results in the local scaling factors  $\gamma_{ki_s} \|\nabla\phi_{i_s}(x_k)\|_2$  to also be bounded from below by  $c_0\rho^{-1}$ . Since they are already bounded from above, the gap between the local scaling factors along any two dimensions is guaranteed to be bounded, the size of which depends on the geometric properties of  $\mathcal{M}$ . The authors ultimately proved that the above construction results in a bilipschitz map  $\Phi_k$  on  $B_k$  whose distortion is at most  $\kappa^2$ , a universal constant which also depends on the geometric properties of  $\mathcal{M}$ . The main challenge in practically realizing the above procedure lies in the estimation of  $\nabla\phi_{i_s}(x_k)^T p_s$ . The next section overcomes this challenge.

### 3. Low-dimensional Low Distortion Local Parameterization

In the procedure to construct  $\Phi_k$  as described above, the selection of the first eigenfunction  $\phi_{i_1}$  relies on the derivative of the eigenfunctions at  $x_k$  along an arbitrary direction  $p_1$ , that is, on  $\nabla\phi_i(x_k)^T p_1$ . In our algorithmic realization of the construction procedure, we take  $p_1$  to be the gradient of an eigenfunction at  $x_k$  itself (say  $\nabla\phi_j(x_k)$ ). We relax the unit norm constraint on  $p_1$ ; note that this will neither affect the math nor the output of our algorithm. Then the selection of  $\phi_{i_1}$  would depend on  $\nabla\phi_i(x_k)^T \nabla\phi_j(x_k)$ . We obtain a numerical estimate of this inner product by making use of the local correlation between the eigenfunctions which was introduced in [12, 13]. These estimates are used to select the subsequent eigenfunctions too.

We first review the local correlation between the eigenfunctions of the Laplacian. In Theorem 2 we show that the limiting value of the scaled local correlation between two eigenfunctions equals the inner product of their gradients. Using this result, we estimate the inner product of the gradients which will be used in Section 3.3 to obtain low distortion local parameterizations of the underlying manifold.

### 3.1. Inner Product of Eigenfunction Gradients using Local Correlation

Let  $(\mathcal{M}, g)$  be a  $d$ -dimensional Riemannian manifold with or without boundary, rescaled so that  $|\mathcal{M}| \leq 1$ . Denote the volume element at  $y$  by  $\omega_g(y)$ . Let  $\phi_i$  and  $\phi_j$  be the eigenfunctions of the Laplacian operator  $\Delta_g$  (see statement of Theorem 1) with eigenvalues  $\lambda_i$  and  $\lambda_j$ . Let  $x_k \in \mathcal{M}$  and define

$$\Psi_{kij}(y) = (\phi_i(y) - \phi_i(x_k))(\phi_j(y) - \phi_j(x_k)). \quad (12)$$

Then the local correlation between the two eigenfunctions  $\phi_i$  and  $\phi_j$  at the point  $x_k$  at scale  $t_k^{-1/2}$  (defined in [12, 13]) is given by

$$A_{kij} = \int_{\mathcal{M}} p(t_k, x_k, y) \Psi_{kij}(y) \omega_g(y), \quad (13)$$

where  $p(t, x, y)$  is the fundamental solution of the heat equation on  $(\mathcal{M}, g)$ . As noted in [12, 13], for  $(t_k, x_k) \in \mathbb{R}_{\geq 0} \times \mathcal{M}$  fixed, we have

$$p(t_k, x_k, y) \sim \begin{cases} t_k^{-d/2} & d_g(x_k, y) \leq t_k^{-1/2} \\ 0 & \text{otherwise} \end{cases} \quad \text{and} \quad \int_{\mathcal{M}} p(t_k, x_k, y) \omega_g(y) = 1. \quad (14)$$

Therefore,  $p(t_k, x_k, \cdot)$  acts as a local probability measure centered at  $x_k$  with scale  $t_k^{-1/2}$  (see Eq. (A.3) in the appendix for a precise form of  $p$ ). We define the scaled local correlation to be the ratio of the local correlation  $A_{kij}$  and a factor of  $2t_k$ .

**Theorem 2.** Denote the limiting value of the scaled local correlation by  $\tilde{A}_{kij}$ ,

$$\tilde{A}_{kij} = \lim_{t_k \rightarrow 0} \frac{A_{kij}}{2t_k}. \quad (15)$$

Then  $\tilde{A}_{kij}$  equals the inner product of the gradients of the eigenfunctions  $\phi_i$  and  $\phi_j$  at  $x_k$ , that is,

$$\tilde{A}_{kij} = \nabla \phi_i(x_k)^T \nabla \phi_j(x_k). \quad (16)$$

A detailed proof is provided in Appendix A. In summary, we choose a sufficiently small  $\epsilon_k$  and show that

$$\lim_{t_k \rightarrow 0} A_{kij} = \lim_{t_k \rightarrow 0} \int_{B_{\epsilon_k}(x_k)} G(t_k, x_k, y) \Psi_{kij}(y) \omega_g(y) \quad (17)$$

where  $B_{\epsilon}(x)$  is defined in Eq. (6) and

$$G(t, x, y) = \frac{e^{-d_g(x, y)^2/4t}}{(4\pi t)^{d/2}}. \quad (18)$$

Then, by using the properties of the exponential map at  $x_k$  and applying basic techniques in calculus, we show that  $\lim_{t_k \rightarrow 0} A_{kij}/2t_k$  evaluates to  $\nabla \phi_i(x_k)^T \nabla \phi_j(x_k)$ .

### 3.2. Estimate of $\tilde{A}_{kij}$ in the discrete setting

To apply Theorems 1 and 2 in practice on data, we need an estimate of  $\tilde{A}_{kij}$  in the discrete setting. The estimation procedure is presented below.

Let  $(x_k)_{k=1}^n$  be uniformly distributed points on  $(\mathcal{M}, g)$ . Let  $d_e(x_k, x'_k)$  be the distance between  $x_k$  and  $x'_k$ . The accuracy with which  $\tilde{A}_{kij}$  can be estimated mainly depends on the accuracy of  $d_e(\cdot, \cdot)$  to the local geodesic distances. For simplicity, we use  $d_e(x_k, x'_k)$  to be the Euclidean distance  $\|x_k - x'_k\|_2$ . A more accurate estimate of the local geodesic distances can be computed using the method described in [14].

We construct a sparse unnormalized graph Laplacian  $L$  using Algo. 1, where the weight matrix  $K$  of the graph edges is defined using the Gaussian kernel. The bandwidth of the Gaussian kernel is set using the local scale of the neighborhoods around each point as in self-tuning spectral clustering [15]. Let  $\phi_i$  be the  $i$ th non-trivial eigenvector of  $L$  and denote  $\phi_i(x_j)$  by  $\phi_{ij}$ .

---

**Algorithm 1:** Sparse Unnormalized Graph Laplacian based on [15]

---

**Input:**  $d_e(x_k, x_{k'})_{k,k'=1}^n, k_{\text{nn}}, k_{\text{tune}}$  where  $k_{\text{tune}} \leq k_{\text{nn}}$   
**Output:**  $L$

- 1  $\mathcal{N}_k \leftarrow$  set of indices of  $k_{\text{nn}}$  nearest neighbours of  $x_k$  based on  $d_e(x_k, \cdot)$ ;
- 2  $\epsilon_k \leftarrow d_e(x_k, x_{k^*})$  where  $x_{k^*}$  is the  $k_{\text{tune}}$ th nearest neighbor of  $x_k$ ;
- 3  $K_{kk} \leftarrow 0, K_{kk'} \leftarrow e^{-d_e(x_k, x_{k'})^2 / \epsilon_k \epsilon_{k'}}, k' \in \mathcal{N}_k$ ;
- 4  $D_{kk} \leftarrow \sum_{k'} K_{kk'}, D_{kk'} \leftarrow 0, k \neq k'$ ;
- 5  $L \leftarrow D - K$ ;

---

We estimate  $\tilde{A}_{kij}$  by evaluating the scaled local correlation  $A_{kij}/2t_k$  at a small value of  $t_k$ . The limiting value of  $A_{kij}$  is estimated by substituting a small  $t_k$  in the finite sum approximation of the integral in Eq. (17). The sum is taken on a discrete ball of a small radius  $\epsilon_k$  around  $x_k$  and is divided by  $2t_k$  to obtain an estimate of  $\tilde{A}_{kij}$ .

We start by choosing  $\epsilon_k$  to be the distance of  $k$ th nearest neighbor of  $x_k$  where  $k$  is a hyperparameter with a small integral value. Thus,

$$\epsilon_k = \text{distance to the } k\text{th nearest neighbor of } x_k. \quad (19)$$

Then the limiting value of  $t_k$  is given by

$$\sqrt{\text{chi2inv}(p, d)}\sqrt{2t_k} = \epsilon_k \implies t_k = \frac{1}{2} \frac{\epsilon_k^2}{\text{chi2inv}(p, d)}, \quad (20)$$

where  $\text{chi2inv}$  is the inverse cdf of the chi-squared distribution with  $d$  degrees of freedom evaluated at  $p$ . We take  $p$  to be 0.99 in our experiments. The rationale behind the above choice of  $t_k$  is described in Appendix B.

Now define the discrete ball around  $x_k$  as

$$U_k = \{x_{k'} \mid d_e(x_k, x_{k'}) \leq \epsilon_k\}. \quad (21)$$

We call  $U_k$  the  $k$ th local view of the data in the high dimensional ambient space. For convenience, denote the estimate of  $G(t_k, x_k, x_{k'})$  by  $G_{kk'}$  where  $G$  is as in Eq. (18). Then

$$G_{kk'} = \begin{cases} \frac{\exp(-d_e(x_k, x_{k'})^2 / 4t_k)}{\sum_{x \in U_k} \exp(-d_e(x_k, x)^2 / 4t_k)} & , x_{k'} \in U_k \\ 0 & , x_{k'} \notin U_k. \end{cases} \quad (22)$$

Finally, the estimate of  $\tilde{A}_{kij}$  is given by

$$\tilde{A}_{kij} = \frac{1}{2t_k} \sum_{x_{k'} \in U_k} G_{kk'} \Psi_{kij}(x_{k'}), \quad (23)$$

where (see Eq. (12))

$$\Psi_{kij}(x_{k'}) = (\phi_{ik'} - \phi_{ik})(\phi_{jk'} - \phi_{jk}). \quad (24)$$



The summation in Eq. (23) corresponds to the finite sum approximation of the integral in Eq. (17) evaluated at the  $t_k$  computed in Eq. (20).

**Example.** This example will follow us throughout the paper. Consider a square grid  $[0, 1] \times [0, 1]$  with a spacing of 0.01 in both  $x$  and  $y$  direction. With  $k_{\text{nn}} = 49$ ,  $k_{\text{tune}} = 7$  and  $d_e(x_i, x_j) = \|x_i - x_j\|_2$  as input to the Algo. 1, we construct the graph Laplacian  $L$ . Using  $k = 25$ ,  $d = 2$  and  $p = 0.99$ , we obtain the discrete balls  $U_k$  and  $t_k$ . Finally, using Eq. (22, 23) with the first two non-trivial eigenvectors  $\phi_1$  and  $\phi_2$  of  $L$ , we obtain the estimate of  $\tilde{A}_{k12}$  as shown in Figure 5. Note that the eigenvectors are a slightly rotated version of the analytic eigenfunctions  $\cos(\pi x)$  and  $\cos(\pi y)$ .

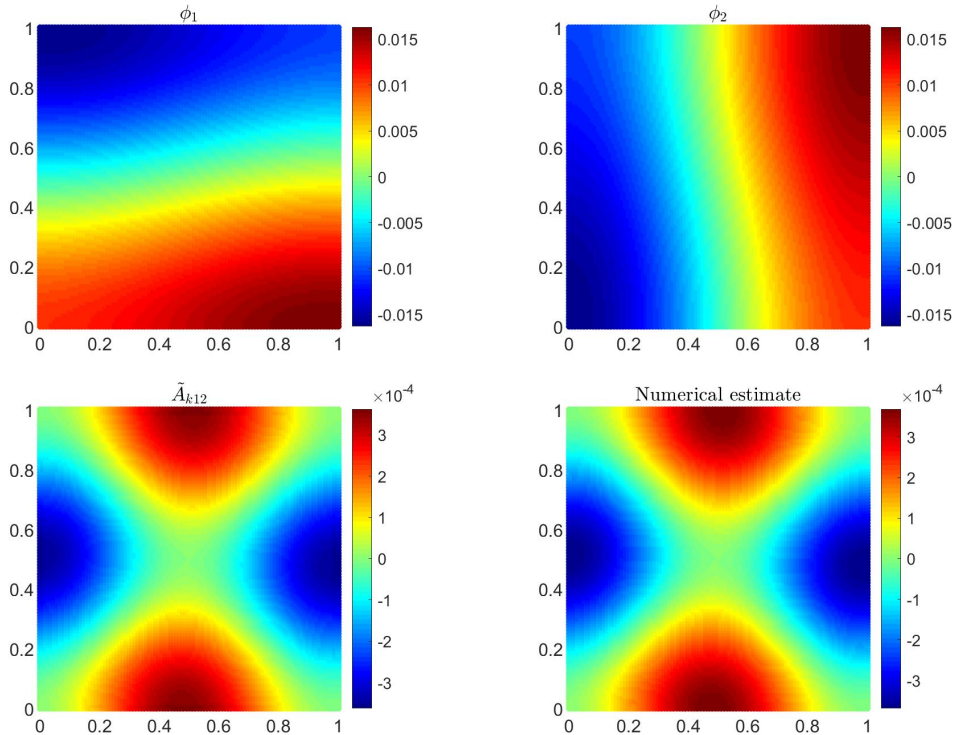


Figure 5: (Top) The first two non-trivial eigenvectors  $\phi_1$  and  $\phi_2$  of the unnormalized graph Laplacian on a square grid. (Bottom) The estimated value of  $\tilde{A}_{k12}$  using the above procedure. Numerically estimated value of  $\nabla\phi_1(x_k)^T\nabla\phi_2(x_k)$ .

### 3.3. Low Distortion Local Parameterization from Laplacian Eigenvectors

Based on the construction procedure following Theorem 1, we compute a set  $S_k$  of eigenvectors to construct low distortion parameterization  $\Phi_k$  of  $U_k$ . There is no easy way to retrieve the set  $S_k$  in the discrete setting as in the procedure. Therefore, we make the natural choice of using the first  $N$  nontrivial eigenvectors  $(\phi_i)_{i=1}^N$  corresponding to the  $N$  smallest eigenvalues  $(\lambda_i)_{i=1}^N$  of the unnormalized graph Laplacian  $L$  as the set  $S_k$ . Therefore, we set  $S_k$  to be  $\{1, \dots, N\}$ . Using the estimates of  $\tilde{A}_{kij}$ , we now present an algorithmic construction of  $\Phi_k$ . The pseudocode is provided below followed by a full explanation of the steps.

---

**Algorithm 2:** BiLipschitz-Local-Parameterization
 

---

**Input:**  $L, N, k, d, p, (\tau_s, \delta_s)_{s=1}^d$   
**Output:**  $(\Phi_k, U_k, \zeta_{kk})_{k=1}^n$   
**1** Compute  $(\phi_i)_{i=1}^N, \lambda_1 \leq \dots \leq \lambda_N$  by eigendecomposition of  $L$ ;  
**2** **for**  $k \leftarrow 1$  **to**  $n$  **do**  
**3**    Compute  $U_k, (\tilde{A}_{kij})_{i,j=1}^N$  (Eq. (21, 23));  
**4**    Compute  $(\gamma_{ki})_{i=1}^N$  (Eq. (7));  
**5**     $\theta_1 \leftarrow \tau_1$ -percentile of  $(\tilde{A}_{kii})_{i=1}^N$ ;  
**6**    Compute  $\tilde{S}_k$  (Eq. (26));  
**7**    Compute  $i_1$  (Eq. (30));  
**8**    **for**  $s \leftarrow 2$  **to**  $d$  **do**  
**9**        Compute  $H_{kij}^s$  (Eq. (32));  
**10**        $\theta_s \leftarrow \tau_s$ -percentile of  $(H_{kii}^s)_{i \in \tilde{S}_k}$ ;  
**11**        Compute  $i_s$  (Eq. (37));  
**12**    **end**  
**13**     $\Phi_k \leftarrow (\gamma_{ki_1} \phi_{i_1}, \dots, \gamma_{ki_d} \phi_{i_d})$  (Eq. (38));  
**14**    Compute  $\zeta_{kk}$  (Eq. (39));  
**15** **end**

---

The estimated value of  $\gamma_{ki}$  is based on the discrete analog of Eq. (7) and is given by

$$\gamma_{ki} = \text{Root-Mean-Square}(\{\phi_{ij} \mid x_j \in U_k\})^{-1}. \quad (25)$$

We use  $\nabla \phi_i \equiv \nabla \phi_i(x_k)$  for brevity. For the stability of our algorithm, the set  $S_k$  is restricted to the indices of the eigenfunctions with sufficiently large gradient, denoted by

$$\tilde{S}_k = S_k \cap \{i : \|\nabla \phi_i\|^2 \geq \theta_1\} = S_k \cap \{i : \tilde{A}_{kii} \geq \theta_1\}, \quad (26)$$

where  $\theta_1$  is  $\tau_1$ -percentile of the set  $\{\tilde{A}_{kii} : i \in S_k\}$  and the second equality follows from Eq. (16). Here  $\tau_1$  is a hyperparameter.

Now we derive a procedure to compute  $\nabla \phi_i^T p_s$  for  $s \in \{1, \dots, d\}$ . The unit norm constraint on  $p_s$  is relaxed. This will neither affect the math nor the output of our algorithm. We start by computing a formula for  $\nabla \phi_i^T p_1$ . We do not know if one exists for an arbitrary  $p_1$ . However, if  $p_1$  is restricted to be the gradient of an eigenvector  $r_1$  ( $\nabla \phi_{r_1}$ ) then using Eq. (16),

$$\nabla \phi_i^T p_1 = \nabla \phi_i^T \nabla \phi_{r_1} = \tilde{A}_{kir_1}. \quad (27)$$

The choice of  $r_1$  will determine  $\phi_{i_1}$ . To obtain a low frequency eigenvector,  $r_1$  is chosen so that the eigenvalue  $\lambda_{r_1}$  is minimal, therefore

$$r_1 = \underset{j \in \tilde{S}_k}{\operatorname{argmin}} \lambda_j. \quad (28)$$

Then we need to find the eigenvector  $\phi_{i_1}$  so that  $\gamma_{ki_1} |\nabla \phi_{i_1}^T p_1|$  is larger than a certain threshold. We do not know what the value of this threshold would be in the discrete setting. Therefore, to obtain a low frequency eigenvector  $\phi_{i_1}$  such that  $\gamma_{ki_1} |\nabla \phi_{i_1}^T p_1|$  is sufficiently large, we first define the maximum possible value of  $\gamma_{ki_1} |\nabla \phi_{i_1}^T p_1|$  using Eq. (27) as

$$\alpha_1 = \max_{i \in \tilde{S}_k} \gamma_{ki} |\nabla \phi_i^T p_1| = \max_{i \in \tilde{S}_k} \gamma_{ki} |\tilde{A}_{kir_1}|. \quad (29)$$

Then we choose  $i_1$

$$i_1 = \underset{i \in \tilde{S}_k}{\operatorname{argmin}} \{ \lambda_i : \gamma_{ki} |\nabla \phi_i^T p_1| \geq \delta_1 \alpha_1 \} = \underset{i \in \tilde{S}_k}{\operatorname{argmin}} \{ \lambda_i : \gamma_{ki} |\tilde{A}_{kir_1}| \geq \delta_1 \alpha_1 \} \quad (30)$$

where  $\delta_1 \in (0, 1]$  is a hyperparameter.

After obtaining  $\phi_{i_1}$ , we move on to obtain the  $s$ -th eigenvector  $\phi_{i_s}$  where  $s \in \{2, \dots, d\}$  in order. First, we need a vector  $p_s$  orthogonal to  $\nabla \phi_{i_1}, \dots, \nabla \phi_{i_{s-1}}$ . For convenience, denote by  $V_s$  the matrix with  $\nabla \phi_{i_1}, \dots, \nabla \phi_{i_{s-1}}$  as columns and let  $\mathcal{R}(V_s)$  be the range of  $V_s$ . Let  $\phi_{r_s}$  be an eigenvector such that  $\nabla \phi_{r_s} \notin \mathcal{R}(V_s)$ . To find such an  $r_s$ , we define

$$H_{kij}^s = \nabla \phi_i^T (I - V_s (V_s^T V_s)^{-1} V_s^T) \nabla \phi_j \quad (31)$$

$$= \tilde{A}_{kij} - \begin{bmatrix} \tilde{A}_{kii_1} & \dots & \tilde{A}_{kii_{s-1}} \end{bmatrix} \begin{bmatrix} \tilde{A}_{ki_1 i_1} & \tilde{A}_{ki_1 i_2} & \dots & \tilde{A}_{ki_1 i_{s-1}} \\ \tilde{A}_{ki_2 i_1} & \tilde{A}_{ki_2 i_2} & \dots & \tilde{A}_{ki_2 i_{s-1}} \\ \vdots & \vdots & \ddots & \vdots \\ \tilde{A}_{ki_{s-1} i_1} & \tilde{A}_{ki_{s-1} i_2} & \dots & \tilde{A}_{ki_{s-1} i_{s-1}} \end{bmatrix}^{-1} \begin{bmatrix} \tilde{A}_{ki_1 j} \\ \tilde{A}_{ki_2 j} \\ \vdots \\ \tilde{A}_{ki_{s-1} j} \end{bmatrix} \quad (32)$$

Note that  $H_{kii}^s$  is the squared norm of the projection of  $\nabla \phi_i$  onto the vector space orthogonal to  $\mathcal{R}(V_s)$ . Clearly  $\nabla \phi_i \notin \mathcal{R}(V_s)$  if and only if  $H_{kii}^s > 0$ . To obtain a low frequency eigenvector  $\phi_{r_s}$  such that  $H_{kr_s r_s}^s > 0$  we choose

$$r_s = \underset{i \in \tilde{S}_k}{\operatorname{argmin}} \{ \lambda_i : H_{kii}^s \geq \theta_s \} \quad (33)$$

where  $\theta_s$  is the  $\tau_s$ -percentile of the set  $\{H_{kii}^s : i \in \tilde{S}_k\}$  and  $\tau_s$  is a hyperparameter. Then we take  $p_s$  to be the component of  $\nabla \phi_{r_s}$  which is orthogonal to  $\mathcal{R}(V_s)$ ,

$$p_s = (I - V_s (V_s^T V_s)^{-1} V_s^T) \nabla \phi_{r_s}. \quad (34)$$

Note that

$$\nabla \phi_i^T p_s = H_{kir_s}^s. \quad (35)$$

To obtain a low frequency eigenvector  $\phi_{i_s}$  such that  $\gamma_{ki_s} |\nabla \phi_{i_s}^T p_s|$  is sufficiently large, we first define the maximum possible value of  $\gamma_{ki_s} |\nabla \phi_i^T p_s|$  using Eq. (35) as,

$$\alpha_s = \max_{i \in \tilde{S}_k} \gamma_{ki} |\nabla \phi_i^T p_s| = \max_{i \in \tilde{S}_k} \gamma_{ki} |H_{kir_s}^s|, \quad (36)$$

and then choose  $i_s$  such that

$$i_s = \underset{i \in \tilde{S}_k}{\operatorname{argmin}} \{ \lambda_i : \gamma_{ki} |\nabla \phi_i^T p_s| \geq \delta_s \alpha_s \} = \underset{i \in \tilde{S}_k}{\operatorname{argmin}} \{ \lambda_i : \gamma_{ki} |H_{kir_s}^s| \geq \delta_s \alpha_s \} \quad (37)$$

where  $\delta_s \in [0, 1]$  is a hyperparameter.

Finally, the  $d$ -dimensional parameterization  $\Phi_k$  of  $U_k$  is given by

$$\begin{aligned} \Phi_k &\equiv (\gamma_{ki_1} \phi_{i_1}, \dots, \gamma_{ki_d} \phi_{i_d}) \text{ where} \\ \Phi_k(x_{k'}) &= (\gamma_{ki_1} \phi_{i_1 k'}, \dots, \gamma_{ki_d} \phi_{i_d k'}) \text{ and} \\ \Phi_k(U_k) &= (\Phi_k(x_{k'}))_{x_{k'} \in U_k}. \end{aligned} \quad (38)$$

We call  $\Phi_k(U_k)$  the  $k$ th local view of the data in the  $d$ -dimensional embedding space. It is a matrix with  $|U_k|$  rows and  $d$  columns. Now, denote the distortion of  $\Phi_{k'}$  on  $U_k$  by  $\zeta_{kk'}$ . Using Eq. (1) we obtain

$$\zeta_{kk'} = \text{Distortion}(\Phi_{k'}, U_k) = \sup_{\substack{x_l, x_{l'} \in U_k \\ x_l \neq x_{l'}}} \frac{\|\Phi_{k'}(x_l) - \Phi_{k'}(x_{l'})\|}{d_e(x_l, x_{l'})} \sup_{\substack{x_l, x_{l'} \in U_k \\ x_l \neq x_{l'}}} \frac{d_e(x_l, x_{l'})}{\|\Phi_{k'}(x_l) - \Phi_{k'}(x_{l'})\|}. \quad (39)$$

The obtained local parameterizations are post-processed so as to remove the anomalous parameterizations having unusually high distortion. We replace the local parameterization  $\Phi_k$  of  $U_k$  by that of a neighbor,  $\Phi_{k'}$  where  $x_{k'} \in U_k$ , if the distortion  $\zeta_{kk'}$  produced by  $\Phi_{k'}$  on  $U_k$  is smaller than  $\zeta_{kk}$ , the distortion produced by  $\Phi_k$  on  $U_k$ . If  $\zeta_{kk'} < \zeta_{kk}$  for multiple  $k'$  then we choose the parameterization which produces the least distortion on  $U_k$ . This procedure is repeated until no replacement is possible. The pseudocode is provided below.

---

**Algorithm 3:** Postprocess-Local-Parameterization

---

**Input:**  $d_e(x_k, x_{k'})_{k, k'=1}^n, (I_k, \Phi_k, \zeta_{kk})_{k=1}^n$   
**Output:**  $(\Phi_k, \zeta_{kk})_{k=1}^n$

```

1  $N_{\text{replaced}} \leftarrow 1$ ;
2 while  $N_{\text{replaced}} > 0$  do
3    $N_{\text{replaced}} \leftarrow 0$ ;
4    $\Phi_k^{\text{old}} \leftarrow \Phi_k$  for all  $k \in \{1, \dots, n\}$ ;
5   for  $k \leftarrow 1$  to  $n$  do
6     Compute  $(\zeta_{kk'})_{x_{k'} \in U_k}$  (Eq. (39));
7      $k^* \leftarrow \underset{x_{k'} \in U_k}{\text{argmin}} \zeta_{kk'}$ ;
8     if  $k^* \neq k$  then
9        $\Phi_k \leftarrow \Phi_{k^*}^{\text{old}}$ ;  $\zeta_{kk} \leftarrow \zeta_{kk^*}$ ;  $N_{\text{replaced}} \leftarrow N_{\text{replaced}} + 1$ ;
10    end
11  end
12 end

```

---

**Example.** We now build upon the example of the square grid at the end of Section 3.1. The values of the additional inputs are  $N = 100$ ,  $\tau_i = 50$  and  $\delta_i = 0.75$  for all  $i \in \{1, \dots, d\}$ . Using Algo. 2 and 3 we obtain  $10^4$  local views  $U_k$  and  $\Phi_k(U_k)$  where  $|U_k| = 25$  for all  $k$ . In the left image of Figure 6, we colored each point  $x_k$  with the distortion  $\zeta_{kk}$  of the local parameterization  $\Phi_k$  on  $U_k$ . The mapped discrete balls  $\Phi_k(U_k)$  for some values of  $k$  are also shown in Figure F.22 in the Appendix.

**Remark 1.** Note that the parameterizations of the discrete balls close to the boundary have higher distortion. This is because the injectivity radius at the points close to the boundary is low and precisely zero at the points on the boundary. As a result, the size of the balls around these points exceeds the limit beyond which Theorem 1 is applicable.

At this point we note the following remark in [6].

**Remark 2.** As was noted by L. Guibas, when  $M$  has a boundary, in the case of Neumann boundary values, one may consider the “doubled” manifold, and may apply the result in Theorem 1 for a possibly larger  $r_k$ .

Due to the above remark, assuming that the points on the boundary are known, we computed the distance matrix for the doubled manifold using the method described in [16]. Then we recomputed the local parameterizations  $\Phi_k$  keeping all other hyperparameters the same as before. In the right image of Figure 6, we colored each point  $x_k$  with the distortion of the updated parameterization  $\Phi_k$  on  $U_k$ . Note the reduction in the distortion on the discs close to the boundary. The corners still have high distortion.

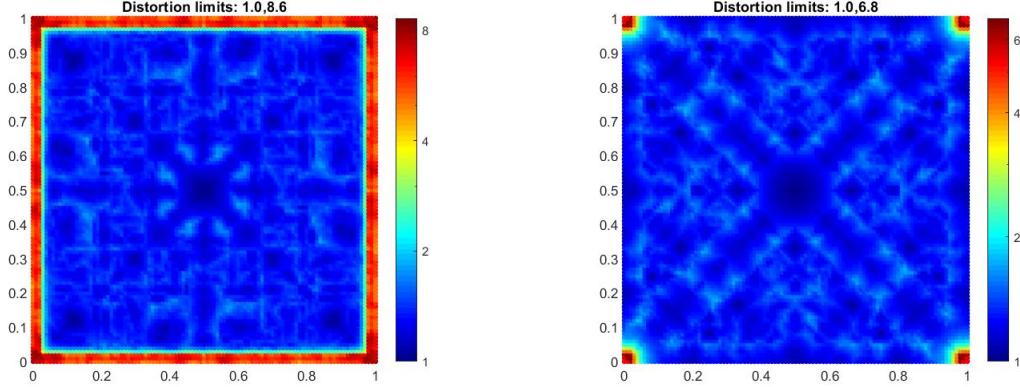


Figure 6: Distortion of the obtained local parameterizations when the points on the boundary are not known (left) versus when they are known apriori (right).

#### 4. Clustering for Intermediate Views

Recall that the discrete balls  $U_k$  are the local views of the data in the high dimensional ambient space. In the previous section, we obtained the mappings  $\Phi_k$  to construct the local views  $\Phi_k(U_k)$  of the data in the  $d$ -dimensional embedding space. In theory, one can use the Generalized Procrustes Analysis (GPA) [17, 18, 19] to register these local views to recover the embedding. In practice, too many small local views (high  $n$  and small  $|U_k|$ ) result in extremely high computational complexity. Moreover, small overlaps between the local views makes their registration susceptible to errors. Therefore, we perform clustering to obtain  $M \ll n$  intermediate views,  $\tilde{U}_m$  and  $\tilde{\Phi}_m(\tilde{U}_m)$ , of the data in the ambient space and the embedding space, respectively. This reduces the time complexity and increases the overlaps between the views, leading to their quick and robust registration.

Our clustering algorithm transforms the notion of a local view per an individual point to an intermediate view per a cluster of points. It is designed so as to ensure low distortion of the parameterizations  $\tilde{\Phi}_m$  on  $\tilde{U}_m$ . We first describe the notation used and then present the pseudocode followed by a full explanation of the steps. Let  $c_k$  be the index of the cluster  $x_k$  belongs to. Then the set of points which belong to cluster  $m$  is given by

$$\mathcal{C}_m = \{x_k \mid c_k = m\}. \quad (40)$$

Denote by  $c_{U_k}$  the set of indices of the neighboring clusters of  $x_k$ . These are the clusters to which the neighbors of  $x_k$  belong. Therefore,

$$c_{U_k} = \{c_{k'} \mid x_{k'} \in U_k\}. \quad (41)$$

Let  $\tilde{U}_m$  be the set of neighboring points of cluster  $m$ . These constitute the neighbors of all the points belonging to cluster  $m$ , that is,

$$\tilde{U}_m = \bigcup_{c_k=m} U_k. \quad (42)$$

We call  $\tilde{U}_m$  the  $m$ th intermediate view of the data in the ambient space. Note that

$$\mathcal{C}_m \subset \tilde{U}_m \text{ and } U_k \subseteq \tilde{U}_{c_k}. \quad (43)$$

Let  $\tilde{\Phi}_m$  be the  $d$ -dimensional parameterization attached with the  $m$ th cluster. This parameterization is used to map  $\tilde{U}_m$  and obtain  $\tilde{\Phi}_m(\tilde{U}_m)$ , the  $m$ th intermediate view of the data in the embedding space.

---

**Algorithm 4:** Clustering

---

**Input:**  $(U_k, \Phi_k)_{k=1}^n, \eta_{\min}$   
**Output:**  $(\mathcal{C}_m, \tilde{U}_m, \tilde{\Phi}_m)_{m=1}^M, (c_k)_{k=1}^n$

- 1 Initialize  $c_k \leftarrow k, \mathcal{C}_m \leftarrow \{x_m\}, \tilde{\Phi}_m \leftarrow \Phi_m$  for all  $k, m \in \{1, \dots, n\}$ ;
- 2 **for**  $\eta \leftarrow 2$  to  $\eta_{\min}$  **do**
- 3     Compute  $\text{cost}_k$  and  $d_k$  for all  $k \in \{1, \dots, n\}$  (Eq. (45, 46));
- 4      $k \leftarrow \underset{j}{\text{argmin}} \text{cost}_j$ ;  $\text{cost}^* \leftarrow \text{cost}_k$ ;
- 5     **while**  $\text{cost}^* < \infty$  **do**
- 6          $s \leftarrow c_k$ ;  $\mathcal{C}_s \leftarrow \mathcal{C}_s \cup x_k$ ;  $c_k \leftarrow d_k$ ;  $\mathcal{C}_{d_k} \leftarrow \mathcal{C}_{d_k} - x_k$ ;
- 7          $\mathcal{S} \leftarrow \{j \mid c_j = d_k \text{ or } d_j = d_k \text{ or } d_j = s \text{ or } s \in c_{U_j}\}$ ;
- 8         Recompute  $\text{cost}_k$  and  $d_k$  for all  $k \in \mathcal{S}$  (Eq. (45, 46));
- 9          $k \leftarrow \underset{j}{\text{argmin}} \text{cost}_j$ ;  $\text{cost}^* \leftarrow \text{cost}_k$ ;
- 10     **end**
- 11 **end**
- 12  $M \leftarrow$  the number of non-empty clusters;
- 13 Remove  $\mathcal{C}_m, \tilde{\Phi}_m$  when  $|\mathcal{C}_m| = 0$ , relabel clusters from 1 to  $M$  and update  $c_k$ ;
- 14 Compute  $(\tilde{U}_m)_{m=1}^M$  (Eq. (42));

---

We initialize the clustering algorithm with  $n$  singleton clusters where the point  $x_k$  belongs to the  $k$ th cluster and the parameterization attached with the  $k$ th cluster is  $\Phi_k$ . Thus,  $c_k = k, \mathcal{C}_m = \{x_m\}$  and  $\tilde{\Phi}_m = \Phi_m$  for all  $k, m \in \{1, \dots, n\}$ . We then move the points around the clusters, updating  $c_k$  and  $\mathcal{C}_m$ , so that at the end of our procedure the size of the resulting non-empty clusters is at least  $\eta_{\min}$ , a hyperparameter. We iterate over  $\eta$  which varies from 2 to  $\eta_{\min}$  such that at the end of each iteration the size of the non-empty clusters is at least  $\eta$ . The size of the non-empty clusters at the start of an iteration is at least  $\eta - 1$ . In a single iteration, we say that the  $m$ th cluster is *small* if it is non-empty and has a size less than  $\eta$ , that is, when  $|\mathcal{C}_m| \in (0, \eta)$ . During an iteration, clusters undergo expansion or contraction as the points in small clusters are moved to neighboring clusters until no small cluster remains. After the last iteration, we prune away all empty clusters.

In a given iteration, we start by selecting a neighboring cluster  $d_k$  for each point to move into and calculate the  $\text{cost}_k$  associated with moving it. The cost function is designed so that the points which are in large clusters are not moved. If  $x_k$  is in a small cluster then the cost of moving it to its neighboring cluster is equal to the distortion produced by the parameterization attached with the cluster on the combined neighbors of  $x_k$  and of the cluster. In other words, the cost function favors the movement of  $x_k$  to its neighboring cluster whose parameterization results in the least distortion on the union of the neighbors of  $x_k$  and the neighbors of the cluster itself. In order to avoid the situation where  $x_k$  continuously oscillates between two clusters, we move  $x_k$  to a cluster which is at least as big as the cluster which  $x_k$  belongs to.

To be more precise, as shown in Figure 7, let  $x_k$  be a point in small cluster. Since  $x_k$  belongs to cluster  $c_k$  therefore  $|\mathcal{C}_{c_k}| \in (0, \eta)$ . Let cluster  $m$  be a neighboring cluster of  $x_k$ , that is  $m \in c_{U_k}$ , such that cluster  $m$  is at least as big as cluster  $c_k$  so that  $|\mathcal{C}_m| \geq |\mathcal{C}_{c_k}|$ . Then the cost of moving  $x_k$  to cluster  $m$  is given by the distortion of  $\tilde{\Phi}_m$  over the combined neighbors of  $x_k$  and the cluster  $m$ , that is  $\text{Distortion}(\tilde{\Phi}_m, U_k \cup \tilde{U}_m)$  (see Eq. (39)). In all other scenarios, the cost is infinity. In the form of an equation, the cost of moving  $x_k$  to cluster  $m$  is

$$\text{cost}_{x_k \rightarrow m} = \begin{cases} \text{Distortion}(\tilde{\Phi}_m, U_k \cup \tilde{U}_m) & \text{if } |\mathcal{C}_{c_k}| \in (0, \eta) \wedge m \in c_{U_k} \wedge |\mathcal{C}_m| \geq |\mathcal{C}_{c_k}| \\ \infty & \text{otherwise.} \end{cases} \quad (44)$$

Then the cost of moving  $x_k$  is

$$\text{cost}_k = \min_m \text{cost}_{x_k \rightarrow m} \quad (45)$$

and the destination cluster to move it into is

$$d_k = \begin{cases} \operatorname{argmin}_m \text{cost}_{x_k \rightarrow m} & \text{if } \text{cost}_k < \infty \\ c_k & \text{otherwise.} \end{cases} \quad (46)$$

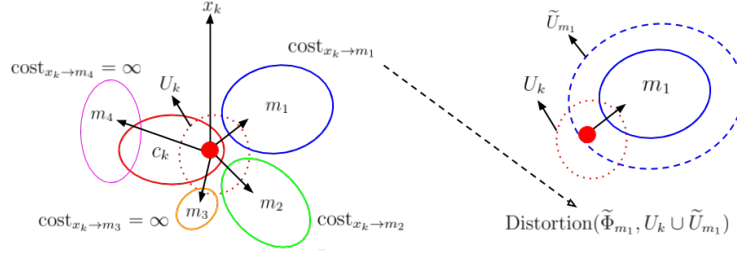


Figure 7: Computation of the cost of moving a point in a small cluster to a neighboring cluster. (left)  $x_k$  is a point represented by a small red disc, in a small cluster  $c_k$  enclosed by solid red line. The dashed red line enclose  $U_k$ . Since cluster  $c_k$  is small,  $|\mathcal{C}_{c_k}| \in (0, \eta)$ . Clusters  $m_1, m_2, m_3$  and  $m_4$  are enclosed by solid colored lines too. Note that  $m_1, m_2$  and  $m_3$  lie in  $c_{U_k}$  (the nonempty overlap between these clusters and  $U_k$  indicate that). Since  $m_4 \notin c_{U_k}$ , the cost of moving  $x_k$  to  $m_4$  is infinity. Since the size of cluster  $m_3$  is less than the size of cluster  $c_k$ ,  $|\mathcal{C}_{m_3}| < |\mathcal{C}_{c_k}|$ , the cost of moving  $x_k$  to cluster  $m_3$  is also infinity. The cost of moving  $x_k$  to clusters  $m_1$  and  $m_2$  are to be computed. (right) The cost of moving  $x_k$  to cluster  $m_1$ ,  $\text{cost}_{x_k \rightarrow m_1}$ , is given by the distortion of  $\tilde{\Phi}_{m_1}$  on  $U_k \cup \tilde{U}_{m_1}$ , where the dashed blue line enclose  $\tilde{U}_{m_1}$ . If  $\text{cost}_{x_k \rightarrow m_1}$  is less (greater) than  $\text{cost}_{x_k \rightarrow m_2}$ , then the destination of  $x_k$  is cluster  $m_1$  ( $m_2$ ) and the associated cost of moving  $x_k$ ,  $\text{cost}_k$ , is  $\text{cost}_{x_k \rightarrow m_1}$  ( $\text{cost}_{x_k \rightarrow m_2}$ ).

Given the cost of moving the points and their destination clusters, we start by picking the point with the minimum cost, say  $x_k$ . As shown in Figure 8, let  $x_k$  be in the cluster  $s$  (note that  $c_k$  is  $s$  before  $x_k$  is moved). We relabel  $c_k$ , the cluster of  $x_k$ , to  $d_k$ , and update the clusters  $\mathcal{C}_s$  and  $\mathcal{C}_{d_k}$  (see Eq. (40)). Since  $x_k$  moved from cluster  $s$  to  $d_k$ , the cost of moving a certain set of points needs to be recomputed. The set of indices of these points is given by  $\mathcal{S}$  where  $j \in \mathcal{S}$  if  $x_j$  either belongs to cluster  $d_k$  ( $c_j = d_k$ ) or has  $d_k$  as the destination cluster ( $d_j = d_k$ ) or has cluster  $s$  as a neighboring cluster ( $s \in c_{U_j}$ ) (see Appendix C for details). After recomputing the cost of moving  $x_j$  and its destination cluster using Eq. (44, 45, 46) for all  $j \in \mathcal{S}$ , we repeat the procedure until the minimum cost becomes infinity indicating that no small component remain.

In the end, let  $M$  be the number of non-empty clusters. We prune away the empty clusters and relabel the non-empty ones from 1 to  $M$  while updating  $c_k$  accordingly, obtaining the clusters  $(\mathcal{C}_m)_{m=1}^M$  with attached parameterizations  $(\tilde{\Phi}_m)_{m=1}^M$ . Finally, using Eq. (42), we obtain the  $M$  intermediate views  $(\tilde{U}_m)_{m=1}^M$  of the data in the ambient space. Then, the intermediate views of the data in the embedding space are given by  $(\tilde{\Phi}_m(\tilde{U}_m))_{m=1}^M$ . Note that  $\tilde{\Phi}_m(\tilde{U}_m)$  is a matrix with  $|\tilde{U}_m|$  rows and  $d$  columns (see Eq. (38)).

**Example.** We continue with our example of the square grid which originally contained about  $10^4$  points. Therefore, before clustering we had about  $10^4$  small local views  $U_k$  and  $\Phi_k(U_k)$ , each containing 25 points. After clustering with  $\eta_{min} = 10$ , we obtained 635 clusters and therefore that many intermediate views  $\tilde{U}_m$  and  $\tilde{\Phi}_m(\tilde{U}_m)$  with an average size of 79. When the points on the boundary are known then we obtained 562 intermediate views with an average size of 90. Note that there is a trade-off between the size of the intermediate views and the distortion of the parameterizations used to obtain them. For convenience, define  $\tilde{\zeta}_{mm}$  to be the distortion of  $\tilde{\Phi}_m$  on  $\tilde{U}_m$  using Eq. (39). Then, as the size of the views are increased (by increasing  $\eta_{min}$ ), the value of  $\tilde{\zeta}_{mm}$  would also increase. In Figure 9 we colored the points in cluster  $m$ ,  $\mathcal{C}_m$ , with  $\tilde{\zeta}_{mm}$ . Note the increased distortion in comparison to Figure 6.

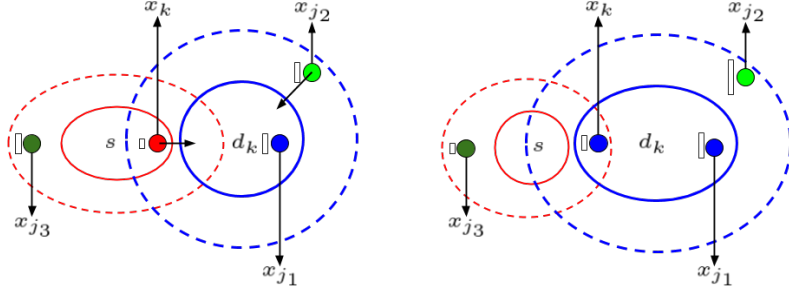


Figure 8: The solid red and blue lines enclose clusters  $s$  and  $d_k$ . The dashed red and blue lines enclose  $\tilde{U}_s$  and  $\tilde{U}_{d_k}$ . Points  $(x_k, x_{j_1}, x_{j_2}$  and  $x_{j_3})$  are represented by small colored discs where the colors indicate the clusters they belong to. Note that  $c_{j_1} = d_k$ ,  $d_{j_2} = d_k$  and  $s \in c_{U_{j_3}}$ . Vertical bars on the left side of these points represent the cost associated with moving them to their destination clusters. (left)  $x_k$  is to be moved from a small cluster  $s$  to cluster  $d_k$ . (right) After moving  $x_k$ , the label (color of disc) of  $x_k$  and the clusters (solid red and blue lines) are updated. The set of their neighboring points (dashed red and blue lines) are intrinsically updated. The destination clusters for the points  $x_k$ ,  $x_{j_1}$ ,  $x_{j_2}$  and  $x_{j_3}$ , and the cost of moving them to their destination clusters are also updated (see Appendix C). Note that  $x_{j_2}$  may no longer have cluster  $d_k$  as the destination.

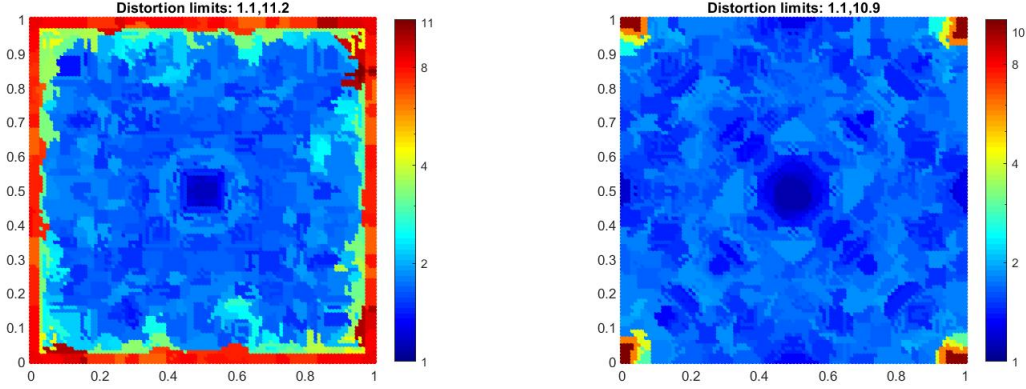


Figure 9: Distortion of the obtained parameterizations of the clusters on the neighboring points of the cluster when the points on the boundary of the square grid are not known (left) versus when they are known apriori (right).

## 5. Global Embedding using Procrustes Analysis

In this section, we present an algorithm based on Procrustes analysis to piece together the intermediate views  $\tilde{\Phi}_m(\tilde{U}_m)$  to obtain a global embedding. The  $M$  views  $\tilde{\Phi}_m(\tilde{U}_m)$  are transformed by an orthogonal matrix  $T_m$  of size  $d \times d$ , a  $d$ -dimensional translation vector  $v_m$  and a positive scalar  $b_m$  as a scaling component. The transformed views are given by  $\tilde{\Phi}_m^g(\tilde{U}_m)$  such that for all  $x_k \in \tilde{U}_m$ ,

$$\tilde{\Phi}_m^g(x_k) = b_m \tilde{\Phi}_m(x_k) T_m + v_m. \quad (47)$$

First we describe a general procedure to estimate these parameters, and its limitations. Then we present an algorithm which computes these parameters and a global embedding of the data, while addressing the limitations of the general procedure. Finally, in Section 5.1 we describe a simple modification to our algorithm to tear apart manifolds without boundary.

In general, the parameters  $(T_m, v_m, b_m)_{m=1}^M$  are estimated so that for all  $m$  and  $m'$ , the two transformed views of the overlap between  $\tilde{U}_m$  and  $\tilde{U}_{m'}$ , obtained using the parameterizations  $\tilde{\Phi}_m^g$  and  $\tilde{\Phi}_{m'}^g$ , align with each other. To be more precise, define the overlap between the  $m$ th and the  $m'$ th intermediate views in the



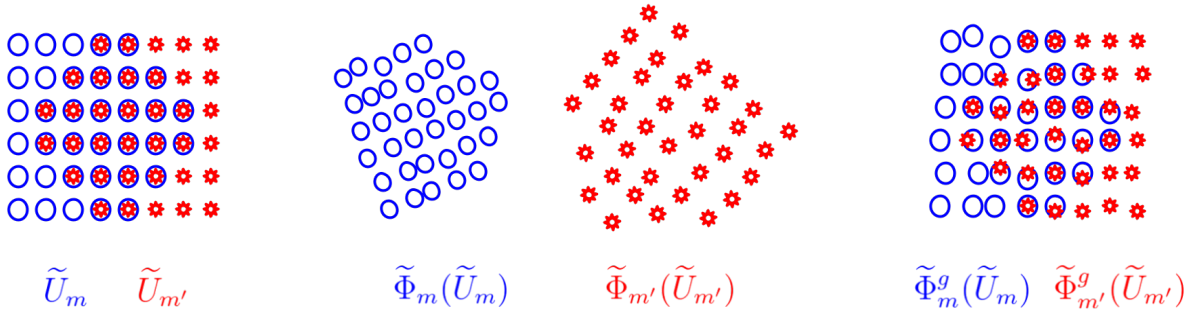


Figure 10: (left) The intermediate views  $\tilde{U}_m$  and  $\tilde{U}_{m'}$  of a 2d manifold in a possibly high dimensional ambient space. These views trivially align with each other. The red star in blue circles represent their overlap  $\tilde{U}_{mm'}$ . (middle) The  $m$ th and  $m'$ th intermediate views in the 2d embedding space. (right) The views after aligning the  $\tilde{\Phi}_m(\tilde{U}_{mm'})$  with  $\tilde{\Phi}_{m'}(\tilde{U}_{mm'})$ .

ambient space as the set of points that are neighbors of both the  $m$ th and  $m'$ th clusters:

$$\tilde{U}_{mm'} = \tilde{U}_m \cap \tilde{U}_{m'}. \quad (48)$$

In the ambient space, the  $m$ th and the  $m'$ th views are neighbors if  $\tilde{U}_{mm'}$  is non-empty. As shown in Figure 10(left), these neighboring views trivially align on the overlap between them. It is natural to ask for a low distortion global embedding of the data. Therefore, we must ensure that the embeddings of  $\tilde{U}_{mm'}$  due to the  $m$ th and the  $m'$ th view in the embedding space, also align with each other. Thus, the parameters  $(T_m, v_m, b_m)_{m=1}^M$  are estimated so that  $\tilde{\Phi}_m^g(\tilde{U}_{mm'})$  aligns with  $\tilde{\Phi}_{m'}^g(\tilde{U}_{mm'})$  for all  $m$  and  $m'$  (see Figure 10). However, due to the distortion of the parameterizations it is usually not possible to perfectly align the two embeddings. We can represent both embeddings of the overlap as matrices with  $|\tilde{U}_{mm'}|$  rows and  $d$  columns. We then measure the error in the alignment as the squared Frobenius norm of the difference of the two matrices. The error is trivially zero if  $\tilde{U}_{mm'}$  is empty. Overall, the estimated parameters minimize the following alignment error

$$\mathcal{L}((T_m, v_m, b_m)_{m=1}^M) = \sum_{m, m'} \left\| \tilde{\Phi}_m^g(\tilde{U}_{mm'}) - \tilde{\Phi}_{m'}^g(\tilde{U}_{mm'}) \right\|_F^2. \quad (49)$$

In theory, one can start with  $T_m$ ,  $v_m$  and  $b_m$  as  $I_d$ ,  $\mathbf{0}$  and 1, and directly use GPA [17, 18, 19] to obtain a local minimum of the above alignment error. This approach has two issues.

1. Like most optimization algorithms, the rate of convergence to a local minimum and the quality of it depends on the initialization of the parameters. With a poor initialization of the parameters, the algorithm may take enormous time to converge and may also converge to an inferior local minimum.
2. Using GPA to align a view with all of its adjacent views would prevent us from tearing apart the manifolds without a boundary; as an example see Figure 11(b).

To address the first issue, we present the pseudocode of our algorithm below followed by a full explanation of the steps. Subsequently, in Section 5.1, to overcome the second issue we present a simple modification of the step R2 in the algorithm.

---

**Algorithm 5:** Calculate-Global-Embedding
 

---

**Input:**  $(x_k, c_k, k)_{k=1}^n, (\mathcal{C}_m, \tilde{\Phi}_m, \tilde{U}_m)_{m=1}^M, \nu$   
**Output:**  $(T_m, b_m, v_m)_{m=1}^M$

- 1 Initialize  $T_m \leftarrow I, v_m \leftarrow 0$ ;
- 2 Compute  $b_m$  (Eq. (50));
- 3 Compute  $(s_m, p_m)_{m=1}^M$  (Eq. (D.5, D.7) in Appendix D);
- 4 **for**  $m \leftarrow 2$  to  $M$  **do**
- 5      $s \leftarrow s_m, p \leftarrow p_m$ ;
- 6     (R1)  $T_s, v_s \leftarrow$  Procrustes  $(\tilde{\Phi}_p^g(\tilde{U}_{sp}), \tilde{\Phi}_s^g(\tilde{U}_{sp}),$  No scaling) [20, 21];
- 7     (R2) Compute  $\mathcal{Z}_s$  (either Eq. (51) or (53));
- 8     (R3)  $\mu_s \leftarrow$  Centroid of  $(\tilde{\Phi}_{m'}^g(\tilde{U}_{sm'}))_{m' \in \mathcal{Z}}$ ;
- 9     (R4)  $T_s, v_s \leftarrow$  Procrustes  $(\mu_s, \tilde{\Phi}_s^g(\cup_{m' \in \mathcal{Z}} \tilde{U}_{sm'}),$  No scaling) [20, 21];
- 10 **end**
- 11 Refine  $(T_m, b_m, v_m)_{m=1}^M$  by executing R1 to R4 for each  $m$  in  $\{1, \dots, M\}$ , several times;
- 12 Compute  $(y_k)_{k=1}^n$  (Eq. (52)).

---

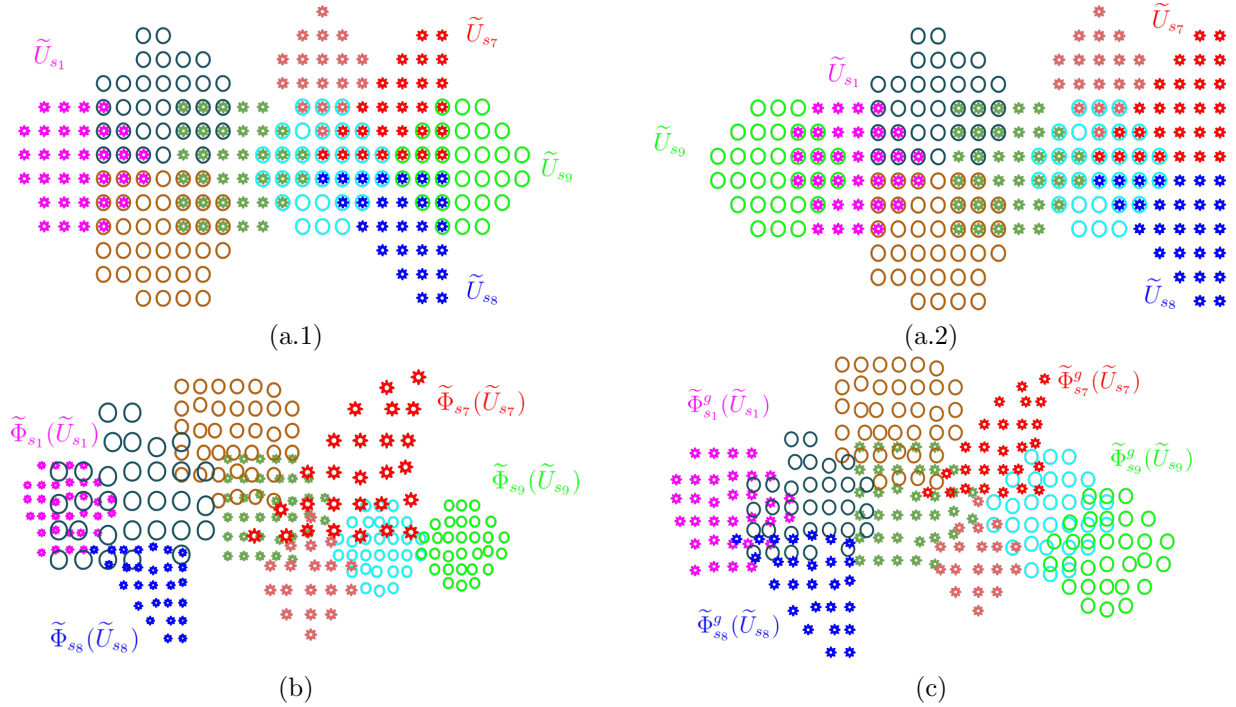


Figure 11: This example will follow us in this section. (a.1 and a.2) Nine intermediate views  $(\tilde{U}_{s_m})_{m=1}^9$  of a 2d manifold are shown when they are placed on a flat plane. In the first case,  $\tilde{U}_{s_9}$  has  $\tilde{U}_{s_7}$  and  $\tilde{U}_{s_8}$  as the only neighboring views among the nine views as shown in (a.1). In the second case, the 2d manifold is assumed to have no boundary in which case there will be at least one view with neighboring views lying far apart on the flat plane. We assume  $\tilde{U}_{s_9}$  to be that view having  $\tilde{U}_{s_1}, \tilde{U}_{s_7}$  and  $\tilde{U}_{s_8}$  as the neighboring views as shown in (a.1) and (a.2). (b) The intermediate views  $(\tilde{\Phi}_{s_m}(\tilde{U}_{s_m}))_{m=1}^9$  in the 2d embedding space, as they were passed as input to the Algo. 5. These views are scrambled in the embedding space and the Algo. 5 will move them to the right location. (c) The transformed views after calculating the scaling  $b_m$  as in Eq. (50).

We initialize with  $T_m = I_d, v_m$  as the zero vector and compute  $b_m$  so as to bring the intermediate views  $\tilde{\Phi}_m(\tilde{U}_m)$  to the same scale as their counterpart  $\tilde{U}_m$  in the ambient space. In turn this brings all the views to similar scale (see Figure 11(c)). We compute the scaling component  $b_m$  to be the ratio of the median

distance between unique points in  $\tilde{U}_m$  and in  $\tilde{\Phi}_k(\tilde{U}_m)$ , that is,

$$b_m = \frac{\text{median} \left\{ d_e(x_k, x_{k'}) \mid x_k, x_{k'} \in \tilde{U}_m, x_k \neq x_{k'} \right\}}{\text{median} \left\{ \left\| \tilde{\Phi}_m(x_k) - \tilde{\Phi}_m(x_{k'}) \right\|_2 \mid x_k, x_{k'} \in \tilde{U}_m, x_k \neq x_{k'} \right\}}. \quad (50)$$

Then we transform the the views in a sequence  $(s_m)_{m=1}^M$ . Let the  $p_m$ th view be the parent of the  $s_m$ th view. The computation of these sequences is described in Appendix D. Here  $p_m$  lies in  $\{s_1, \dots, s_{m-1}\}$  and it is a neighboring view of the  $s_m$ th view in the ambient space, that is,  $\tilde{U}_{s_m p_m}$  is non-empty. The first view in the sequence ( $s_1$ th view) is not transformed, therefore  $T_{s_1}$  and  $v_{s_1}$  are not updated. We then iterate over  $m$  which varies from 2 to  $M$ . For convenience, denote  $s_m$  by  $s$  and  $p_m$  by  $p$ . To update  $T_s$  and  $v_s$ , the following four step procedure is followed.

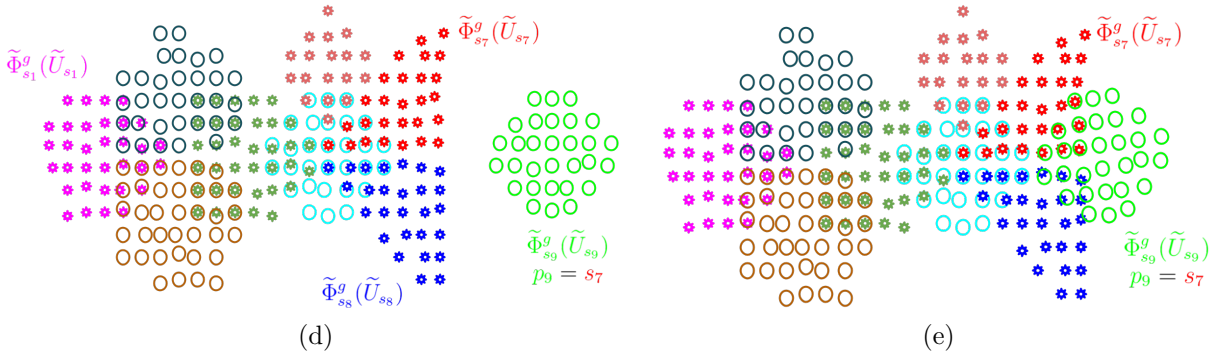


Figure 12: In continuation of Figure 11. (d) The transformed intermediate views  $(\tilde{\Phi}_{s_m}^g(\tilde{U}_{s_m}))_{m=1}^9$  before the start of the iteration  $m = 9$  are shown. (e) Assuming  $p_9 = s_7$ , in step R1,  $T_{s_9}$  and  $v_{s_9}$  are computed so that the view  $\tilde{\Phi}_{s_9}^g(\tilde{U}_{s_9})$  aligns with the view  $\tilde{\Phi}_{s_7}^g(\tilde{U}_{s_7})$ . The resulting transformed view  $\tilde{\Phi}_{s_9}^g(\tilde{U}_{s_9})$  is shown. Note that step R1 results in the same output for both cases described in Figure 11.

**Step R1.** We compute a temporary value of  $T_s$  and  $v_s$  by aligning the views  $\tilde{\Phi}_s^g(\tilde{U}_{sp})$  and  $\tilde{\Phi}_p^g(\tilde{U}_{sp})$  of the overlap  $\tilde{U}_{sp}$ , using Procrustes analysis [20, 21] without modifying  $b_s$  (see Figure 12).

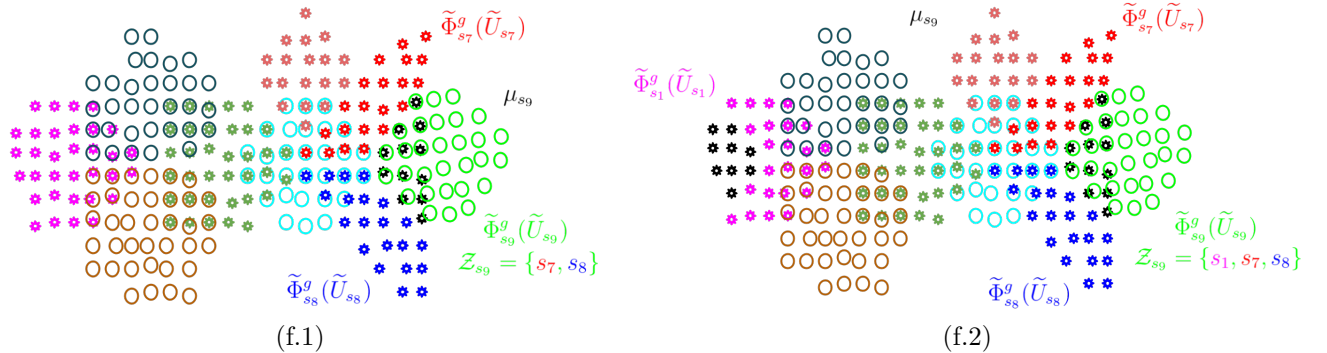


Figure 13: In continuation of Figures 11 and 12. In the first case as described in the caption of Figure 11, among the nine views,  $\tilde{U}_{s_9}$  has non-empty overlaps with  $\tilde{U}_{s_7}$  and  $\tilde{U}_{s_8}$  only. Therefore, step R2 results in  $\mathcal{Z}_{s_9} = \{s_7, s_8\}$  and the  $\mu_{s_9}$  obtained in step R3 is shown in black in (f.1). On the other hand, in the second case when the manifold is without a boundary,  $\tilde{U}_{s_9}$  has non-empty overlaps with  $\tilde{U}_{s_1}$ ,  $\tilde{U}_{s_7}$  and  $\tilde{U}_{s_8}$ . Therefore, in this case, step R2 results in  $\mathcal{Z}_{s_9} = \{s_1, s_7, s_8\}$  and the  $\mu_{s_9}$  obtained in step R3 is again shown in black in (f.2).

**Step R2.** Then we identify more views to align the  $s$ th view with. We compute a subset  $\mathcal{Z}_s$  of  $\{s_1, \dots, s_{m-1}\}$ , the indices of already aligned  $m-1$  views, such that  $m' \in \mathcal{Z}_s$  if the  $s$ th view and the  $m'$ th view are neighbors

in the ambient space (see Figure 13). Therefore,

$$\mathcal{Z}_s = \{m' \mid \tilde{U}_{sm'} \neq \emptyset\} \cap \{s_1, \dots, s_{m-1}\}. \quad (51)$$

**Step R3.** We then compute the centroid  $\mu_s$  of the views  $(\tilde{\Phi}_{m'}^g(\tilde{U}_{sm'}))_{m' \in \mathcal{Z}_s}$  (see Figure 13). Here  $\mu_s$  is a matrix with  $d$  columns and the number of rows given by the size of the set  $\cup_{m' \in \mathcal{Z}_s} \tilde{U}_{sm'}$ . A point in this set can have multiple embeddings due to multiple parameterizations  $(\tilde{\Phi}_{m'}^g)_{m' \in \mathcal{Z}_s}$  depending on the overlaps  $(\tilde{U}_{sm'})_{m' \in \mathcal{Z}_s}$  it lies in. The mean of these embeddings forms a row in  $\mu_s$ .

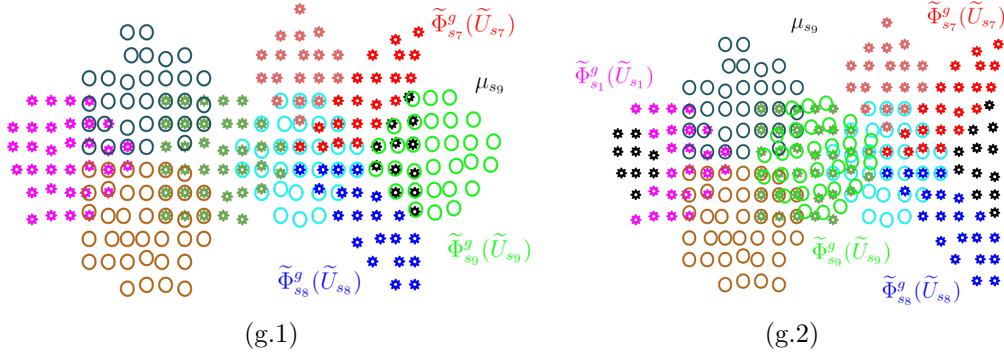


Figure 14: In continuation of Figures 11-13. For the first case, in step R4,  $T_{s_9}$  and  $v_{s_9}$  are updated so that the view  $\tilde{\Phi}_{s_9}^g(\tilde{U}_{s_9s_7} \cup \tilde{U}_{s_9s_8})$  aligns with  $\mu_{s_9}$ . The resulting view  $\tilde{\Phi}_{s_9}^g(\tilde{U}_{s_9})$  is shown in (g.1). In the second case when the manifold has no boundary,  $T_{s_9}$  and  $v_{s_9}$  are updated in step R4 so that the view  $\tilde{\Phi}_{s_9}^g(\tilde{U}_{s_9s_1} \cup \tilde{U}_{s_9s_7} \cup \tilde{U}_{s_9s_8})$  aligns with  $\mu_{s_9}$ . The resulting view  $\tilde{\Phi}_{s_9}^g(\tilde{U}_{s_9})$  is shown in (g.2), which is not a desired output as it sets off the distortion of the global embedding. We resolve this issue in Section 5.1.

**Step R4.** Finally, we update  $T_s$  and  $v_s$  by aligning the view  $\tilde{\Phi}_s^g(\tilde{U}_{sm'})$  with  $\tilde{\Phi}_{m'}^g(\tilde{U}_{sm'})$  for all  $m' \in \mathcal{Z}_s$ . This alignment is based on the approach in [17, 18] where, using the Procrustes analysis [20, 21], the view  $\tilde{\Phi}_s^g(\cup_{m' \in \mathcal{Z}_s} \tilde{U}_{sm'})$  is aligned with the centroid  $\mu_s$ , without modifying  $b_s$  (see Figure 14).

To further refine the parameters  $(T_m, v_m, b_m)_{m=1}^M$  we iterate over all the views in random order and perform steps R2, R3 and R4 in Algo. 5. We repeat this procedure several times without refining  $b_m$  in the Procrustes algorithm [17, 21] and then with refining  $b_m$  (in this case, the Procrustes method in step R4 will return an additional output  $b_s$ ). In the end, we compute the global embedding  $y_k$  of  $x_k$  by mapping  $x_k$  using the transformed parameterization attached with the cluster  $c_k$  it belongs to,

$$y_k = \tilde{\Phi}_{c_k}^g(x_k). \quad (52)$$

### 5.1. Tearing manifolds without boundary

When the manifold has no boundary, then the step R2 in Algo. 5 may result in a set  $\mathcal{Z}_s$  containing the indices of the views which are neighbors of the  $s$ th view in the ambient space but are far apart from the transformed  $s$ th view in the embedding space, obtained right after step R1. For example, as shown in Figure 13 (f.2),  $s_1 \in \mathcal{Z}_{s_9}$  because the  $s_9$ th view and the  $s_1$ th view are neighbors in the ambient space (see Figure 11 (a.1, a.2)) but in the embedding space, they are far apart. Due to such indices in  $\mathcal{Z}_{s_9}$ , the step R3 results in a centroid, which when used in step R4, results in a fallacious estimation of the parameters  $T_s$  and  $v_s$ , giving rise to a high distortion embedding. By trying to align with all its neighbors in the ambient space, the  $s_9$ th view is misaligned with respect to all of them (see Figure 14 (g.2)).

Therefore we modify the step R2 so as to include the indices of only those views in the set  $\mathcal{Z}_s$  which are neighbors of the  $s$ th view in both the ambient space as well as in the embedding space. We denote the

overlap between the  $m$ th and  $m'$ th view in the embedding space by  $\tilde{U}_{mm'}^g$ . There may be multiple heuristics for computing  $\tilde{U}_{mm'}^g$ , which could work. In the Appendix E, we describe a simple approach based on the already developed machinery in this paper. Having obtained  $\tilde{U}_{mm'}^g$ , we say that the  $m$ th and the  $m'$ th intermediate views in the embedding space are neighbors if  $\tilde{U}_{mm'}^g$  is non-empty.

**Step R2 updated.** Finally, we compute  $\mathcal{Z}_s$  as,

$$\mathcal{Z}_s = \{m' \mid \tilde{U}_{sm'} \neq \emptyset, \tilde{U}_{sm'}^g \neq \emptyset\} \cap \{s_1, \dots, s_{m-1}\}. \quad (53)$$

Note that if it is known apriori that the manifold can be embedded in lower dimension without tearing it apart then we do not require the above modification. In all of our experiments except the one in Section 6.3, we do not assume that this information is available.

With this modification, the set  $\mathcal{Z}_{s_9}$  in Figure 13 (f.2) will not include  $s_1$  and therefore the resulting centroid in the step R3 would be the same as the one in Figure 13 (f.1). Subsequently, the transformed  $s_9$ th view would be the one in Figure 14 (g.1) rather than Figure 14 (g.2).

Having knowingly torn the manifold apart, we provide at the output, information on the points belonging to the tear and their neighboring points in the ambient space. To encode the “gluing” instructions along the tear in the form of colors at the output of our algorithm, we recompute  $\tilde{U}_{mm'}^g$ . If  $\tilde{U}_{mm'}^g$  is non-empty but  $\tilde{U}_{mm'}^g$  is empty, then this means that the  $m$ th and  $m'$ th views are neighbors in the ambient space but are torn apart in the embedding space. Therefore, we color the global embedding of the points on the overlap  $\tilde{U}_{mm'}^g$  with the same color to indicate that although these points are separated in the embedding space, they are adjacent in the ambient space (see Figures 19, 20 and F.23).

**Example.** The obtained global embeddings of our square grid with  $\nu = 3$  as in the Appendix E, are shown in Figure 15. Note that the boundary of the obtained embedding is more distorted when the points on the boundary are unknown than when they are known apriori. This is because the intermediate views near the boundary have higher distortion in the former case than in the latter case (see Figure 9).

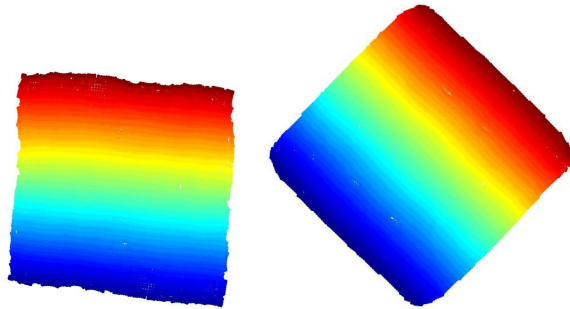


Figure 15: Global embedding of the square grid when the points on the boundary are unknown (left) versus when they are known apriori (right).

## 6. Experimental Results

We present experiments to compare LDLE with UMAP [5], t-SNE [4] and Laplacian eigenmaps [3] on several datasets. These datasets are discretized 2d manifolds embedded in  $\mathbb{R}^2$ ,  $\mathbb{R}^3$  or  $\mathbb{R}^4$ , containing about  $10^4$  points. These manifolds can be grouped based on the presence of the boundary and their orientability, as shown in Figures 16, 19 and 20. The inputs are shown in the figures themselves except for the flat torus and

the Klein bottle, as their 4D parameterizations cannot be plotted. Therefore, we describe their construction below.

**Flat Torus.** A flat torus is a parallelogram whose opposite sides are identified. In our case, we construct a discrete flat torus using a rectangle with sides 2 and 0.5 and embed it in four dimensions as follows,

$$X(\theta_i, \phi_j) = \frac{1}{4\pi}(4\cos(\theta_i), 4\sin(\theta_i), \cos(\phi_j), \sin(\phi_j)) \quad (54)$$

where  $\theta_i = 0.01i\pi$ ,  $\phi_j = 0.04j\pi$ ,  $i \in \{0, \dots, 199\}$  and  $j \in \{0, \dots, 49\}$ .

**Klein bottle.** A Klein bottle is a non-orientable two dimensional manifold without boundary. We construct a discrete Klein bottle using its 4D Möbius tube representation as follows,

$$X(\theta_i, \phi_j) = (R(\phi_j) \cos \theta_i, R(\phi_j) \sin \theta_i, r \sin \phi_j \cos \frac{\theta_i}{2}, r \sin \phi_j \sin \frac{\theta_i}{2}) \quad (55)$$

$$R(\phi_j) = R + r \cos \phi_j \quad (56)$$

where  $\theta_i = i\pi/100$ ,  $\phi_j = j\pi/25$ ,  $i \in \{0, \dots, 199\}$  and  $j \in \{0, \dots, 49\}$ .

### 6.1. Hyperparameters

To embed using LDLE, for all the examples, we use the Euclidean metric,  $k_{\text{nn}} = 49$ ,  $k_{\text{tune}} = 7$ ,  $N = 100$ ,  $d = 2$ ,  $p = 0.99$ ,  $k = 25$ ,  $\tau_i = 50$ ,  $\delta_i = 0.9$ ,  $\nu = 3$ ,  $N_r = 100$ . Only the value of  $\eta_{\text{min}}$  varies across the examples and is provided in the Table F.1.

For UMAP, t-SNE and Laplacian eigenmaps, we use the Euclidean metric and select the hyperparameters by grid search, choosing the values which result in best visualization quality. For UMAP, we use 500 epochs and search for optimal `n_neighbors` in  $\{25, 50, 100, 200\}$  and `min_dist` in  $\{0.01, 0.1, 0.25, 0.5\}$ . For t-SNE, we use 1000 iterations and search for optimal perplexity in  $\{30, 40, 50, 60\}$  and early exaggeration in  $\{2, 4, 6\}$ . For Laplacian eigenmaps, we search for  $k_{\text{nn}}$  in  $\{16, 25, 36, 49\}$  and  $k_{\text{tune}}$  in  $\{3, 7, 11\}$ . The chosen values of the hyperparameters are provided in Table F.1. We note that the Laplacian eigenmaps fails to correctly embed most of the examples regardless of the choice of the hyperparameters.

### 6.2. Results

In Figure 16, we show the 2d embeddings of 2d manifolds with boundary, in  $\mathbb{R}^2$  or  $\mathbb{R}^3$ . To a large extent, LDLE preserved the shape of the holes. UMAP and Laplacian eigenmaps distorted the shape of the holes and the region around them, while t-SNE produced dissected embeddings. For the sphere with a hole which is a curved 2d manifold with boundary, embedded in  $\mathbb{R}^3$ , both UMAP and Laplacian eigenmaps squeezed it into  $\mathbb{R}^2$  while LDLE and t-SNE tore it apart. The correctness of the LDLE embedding is proved in Figure F.23.

We note that the boundaries of the LDLE embeddings in Figure 16 are usually distorted. The cause of this is explained in Remark 1. When the points in the input which lie on the boundary are known apriori then the distortion near the boundary can be reduced using the doubled manifold as discussed in Remark 2 and shown in Figure 5. The obtained LDLE embeddings when the points on the boundary are known, are shown in Figure 17.

To compare the embeddings in a quantitative manner, we plot the distortion of the geodesics originating from each point in the input in Figure 18. In the discrete setting, we take the geodesic between two given points as the shortest path between them. Using Dijkstra algorithm over a graph of 5 nearest neighbors with  $d_e$  as the underlying metric, we compute the sequence of nodes on the shortest path between  $x_k$  and



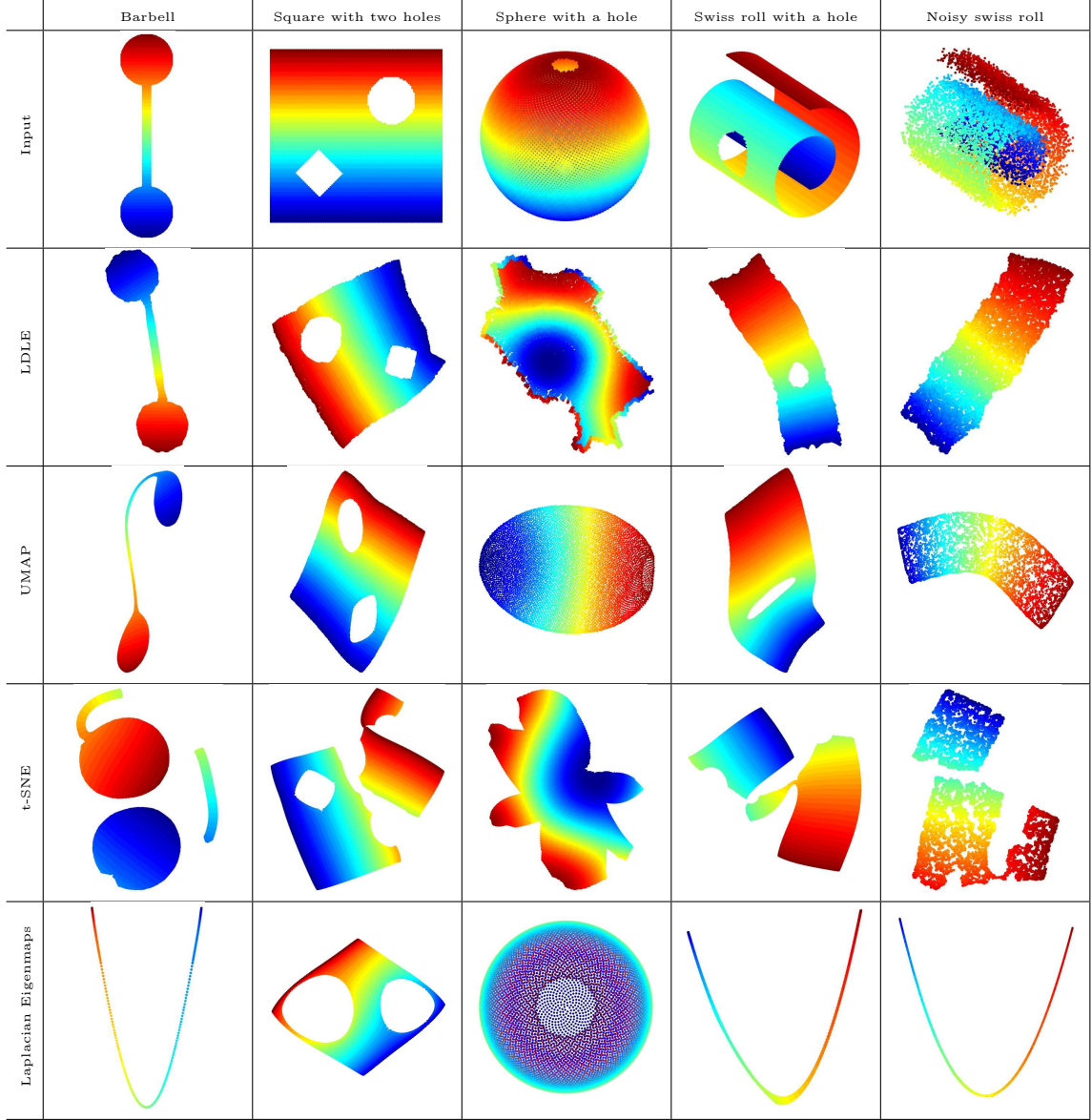


Figure 16: Embeddings of 2d manifolds with boundary into  $\mathbb{R}^2$ . The noisy swiss roll is constructed by adding uniform noise in all three dimensions, with support on  $[0, 0.05]$ .

$x_{k'}$ . Denote the number of nodes on this path by  $n_{kk'}$ , the sequence of nodes by  $(x_{kk'_s})_{s=1}^{n_{kk'}}$  and the length of the path in the input space by

$$L_{kk'} = \sum_{s=2}^{n_{kk'}} d_e(x_{kk'_s}, x_{kk'_{s-1}}). \quad (57)$$

Denote the embedding of  $x_k$  by  $y_k$ . Then the length of the shortest path between  $x_k$  and  $x_{k'}$  in the embedding space is given by

$$L_{kk'}^g = \sum_{s=2}^{n_{kk'}} d_e(y_{kk'_s}, y_{kk'_{s-1}}). \quad (58)$$

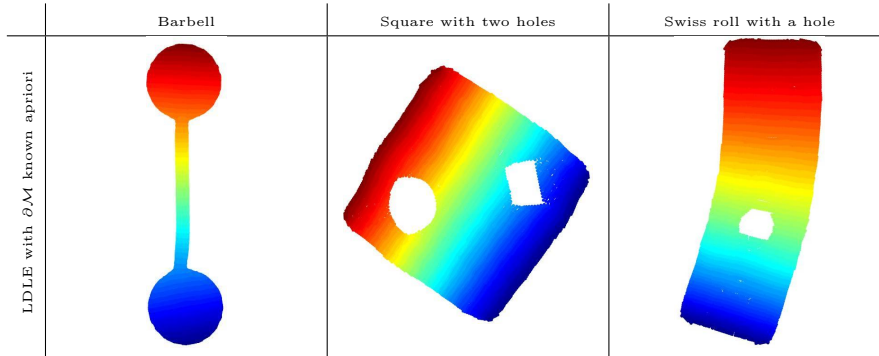


Figure 17: LDLE embeddings when the points on the boundary are known apriori.

Finally, the distortion of the paths originating from  $x_k$  is given by

$$\mathcal{D}_k = \sup_{k'} \frac{L_{kk'}^g}{L_{kk'}} \sup_{k'} \frac{L_{kk'}}{L_{kk'}^g}. \quad (59)$$

Compared to the other algorithms, the global embedding produced by LDLE least distorts the shortest geodesics in the input space, especially when the points on the boundary are known apriori.

In Figure 19, we show the 2d embeddings of 2d manifolds without boundary, a curved torus in  $\mathbb{R}^3$  and a flat torus in  $\mathbb{R}^4$ . LDLE produced similar representation for both the inputs. None of the other methods do that. The main difference in the LDLE embedding of the two inputs is based on the length of the same colored pieces of the boundary. Note that these pieces are adjacent in the input space. For the flat torus, the two pieces with same colors are almost equal in length while for the curved torus, they usually have different lengths. This is because of the difference in the curvature of the two inputs, zero everywhere for the flat torus and non-zero almost everywhere on the curved torus. The mathematical correctness of the LDLE embeddings using the cut and paste argument is shown in Figure F.23.

In Figure 20, we show the 2d embeddings of non-orientable 2d manifolds, a Möbius strip in  $\mathbb{R}^3$  and a Klein bottle in  $\mathbb{R}^4$ . Laplacian eigenmaps produced incorrect embeddings, t-SNE produced dissected and non-interpretable embeddings and UMAP squeezed the inputs into  $\mathbb{R}^2$ . On the other hand, LDLE produced mathematically correct embeddings by tearing apart both inputs to embed them into  $\mathbb{R}^2$ .

### 6.3. High Dimensional Data

In Figure 21, motivated from [22], we embed a 42 dimensional synthetic data set representing the signal strength of 42 transmitters at about  $n = 6000$  receiving locations on a toy floor plan. The transmitters and the receivers are distributed uniformly across the floor. Let  $(t_{r_k})_{k=1}^{42}$  be the transmitter locations and  $r_i$  be the  $i$ th receiver location. Then the  $i$ th data point  $x_i$  is given by  $(e^{-\|r_i - t_{r_k}\|_2})_{k=1}^{42}$ . The resulting data set is embedded into  $\mathbb{R}^2$  using LDLE, UMAP, t-SNE and Laplacian eigenmaps. The hyperparameters are set in the same way as in the above examples (see Table F.1) except for  $\nu$  in Algo. 5, which is set to infinity since we know apriori that the data does not represent a manifold without boundary. The obtained embeddings are shown in Figure 21. The shapes of the holes are better preserved by LDLE than the other algorithms but the corners of the LDLE embedding are more distorted. The reason for distorted corners is given in Remark 1.

## 7. Conclusions and Future Directions

We have presented a new bottom-up approach (LDLE) for manifold learning which constructs low-dimensional low distortion local parameterizations of the data and registers them to obtain a global embedding. We



demonstrated on various examples that LDLE competes with the other methods in terms of visualization quality. In particular, the embeddings produced by LDLE are geometrically more accurate than those produced by UMAP, t-SNE and Laplacian Eigenmaps. We also demonstrated that LDLE can embed manifolds without boundary as well as non-orientable manifolds into their intrinsic dimension, a feature that is missing from the existing techniques.

Some of the future directions of our work are as follows.

- It is natural to expect a manifold learning technique to fall back to clustering when the data in high dimension does not represent a low dimensional manifold. Therefore, we aim to augment LDLE so as to obtain global embedding of clustered data (at multiple resolutions) as in [23].
- As observed in the experimental results, when the boundary of the manifold is known apriori, then the global embedding tend to also have low distortion near the boundary. We aim to develop a method based on [24] to approximately calculate the boundary of the manifold and analyze LDLE results using the doubled manifold along the estimated boundary.
- The spectrum of the Laplacian has been used in prior work for anomaly detection [25, 26, 27, 28]. In [29, 27], subsets of Laplacian eigenvectors were identified so as to separate small clusters from a large background component. In our case, the local views built using Laplacian eigenfunctions, which have unusually high distortion may point to the presence of anomalous data points in that view. We aim to further investigate this direction to develop an anomaly detection technique.

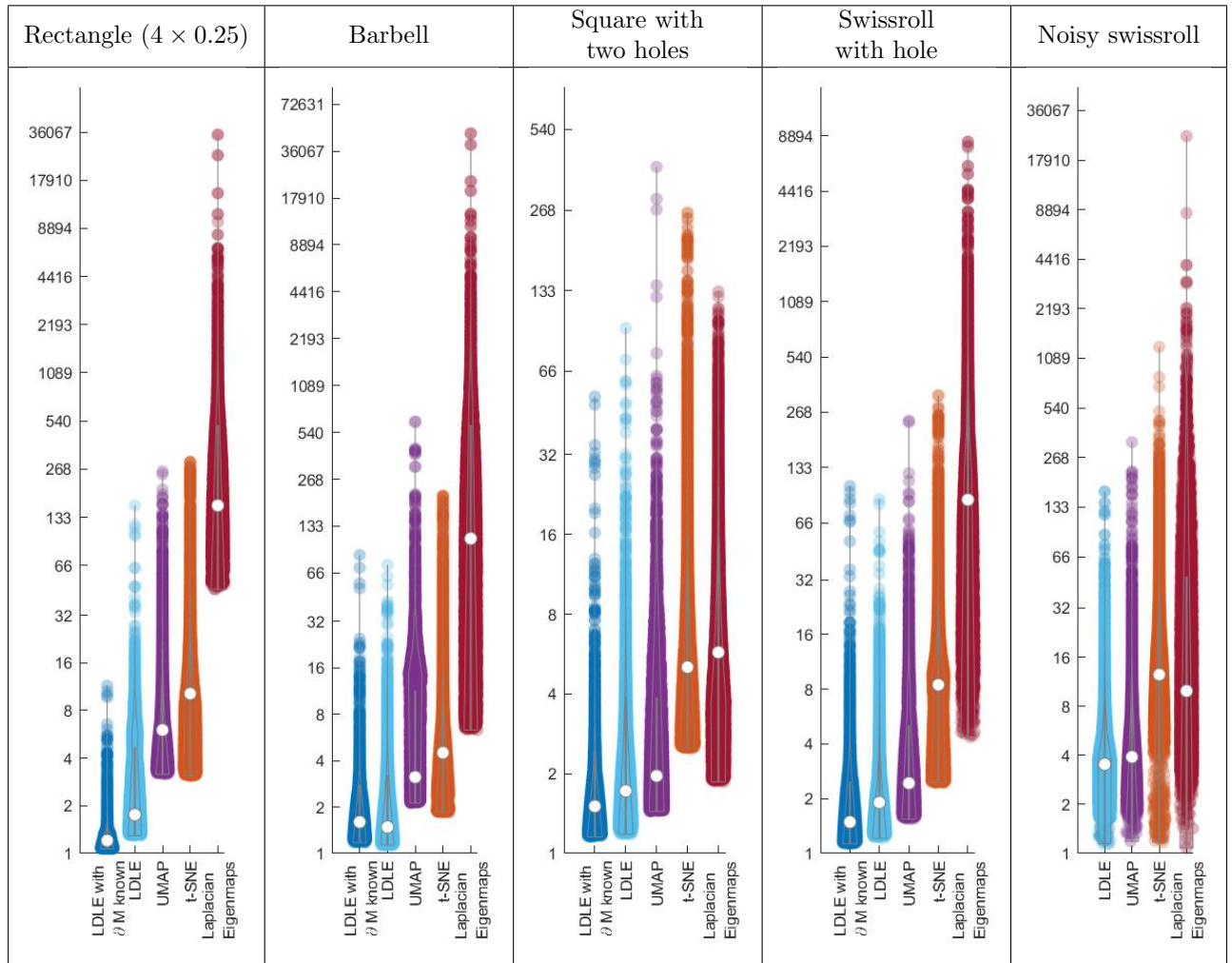


Figure 18: Distortion of the geodesics originating from each point in the input (See Eq. (59)).

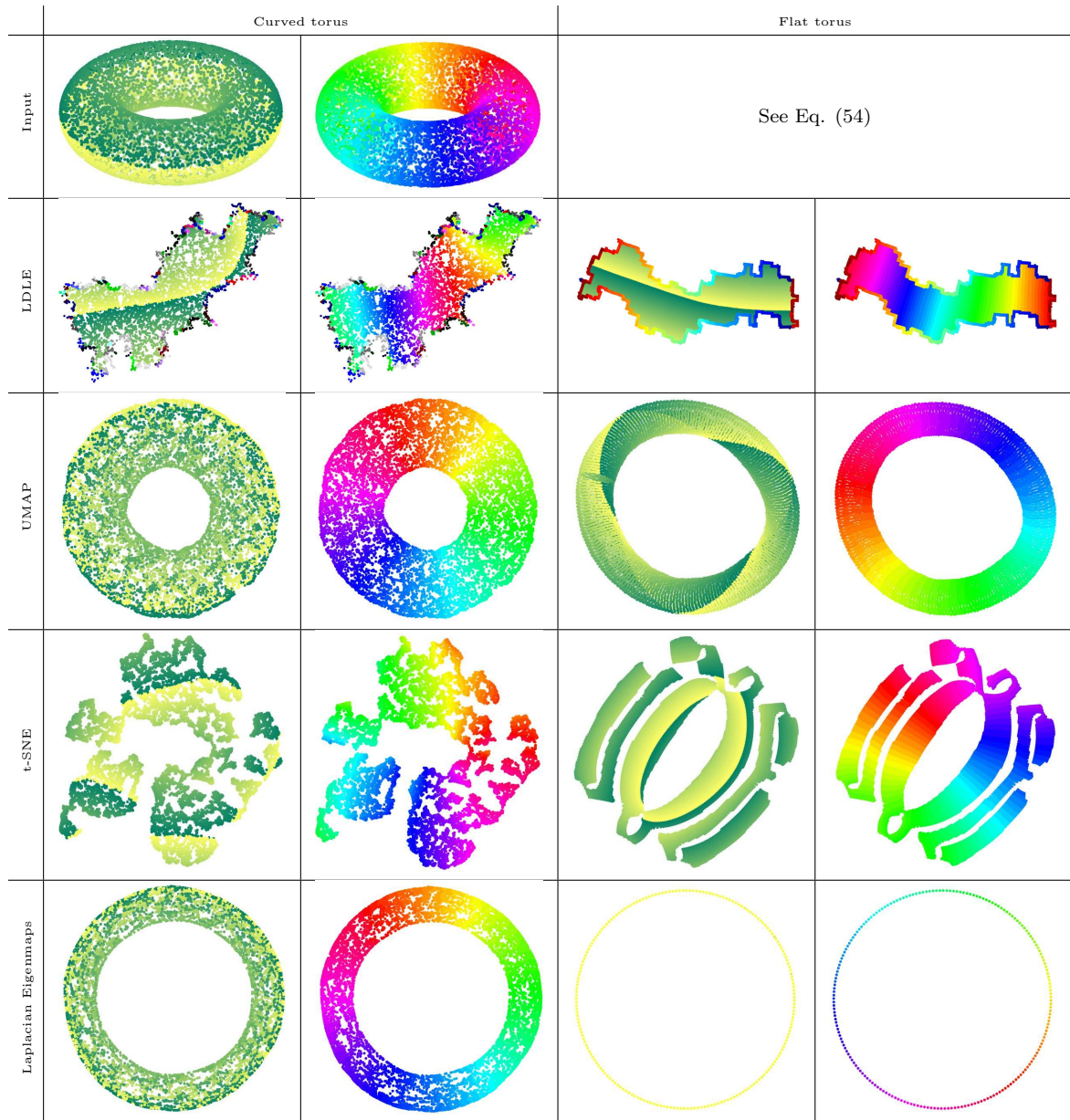


Figure 19: Embeddings of 2d manifolds without boundary into  $\mathbb{R}^2$ . For each manifold, the left and right columns contain the same plots colored by the two parameters of the manifold. A proof of the mathematical correctness of the LDLE embeddings is provided in Figure F.23.

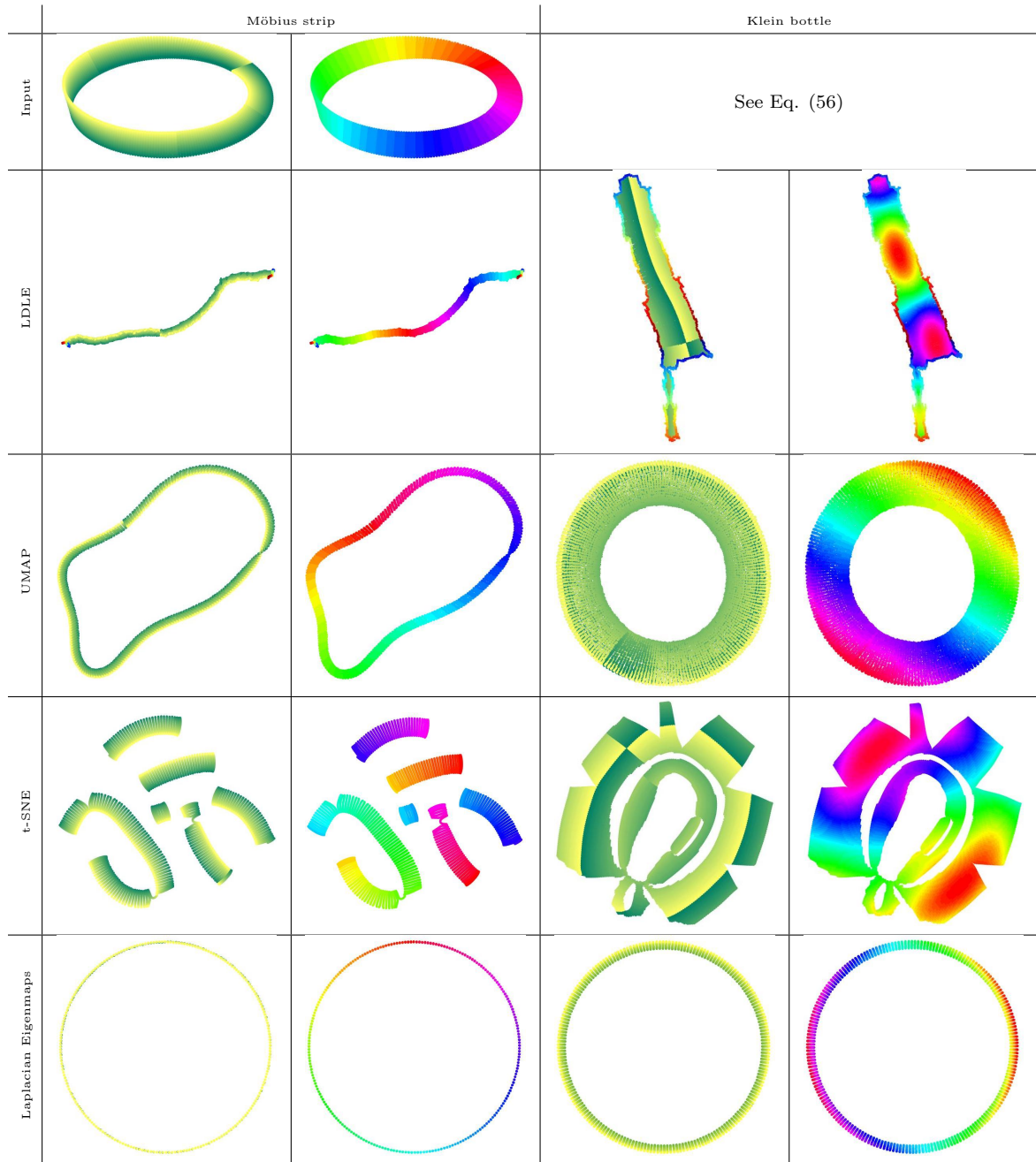


Figure 20: Embeddings of 2d non-orientable manifolds into  $\mathbb{R}^2$ . For each manifold, the left and right columns contain the same plots colored by the two parameters of the manifold. A proof of the mathematical correctness of the LDLE embeddings is provided in Figure F.23.

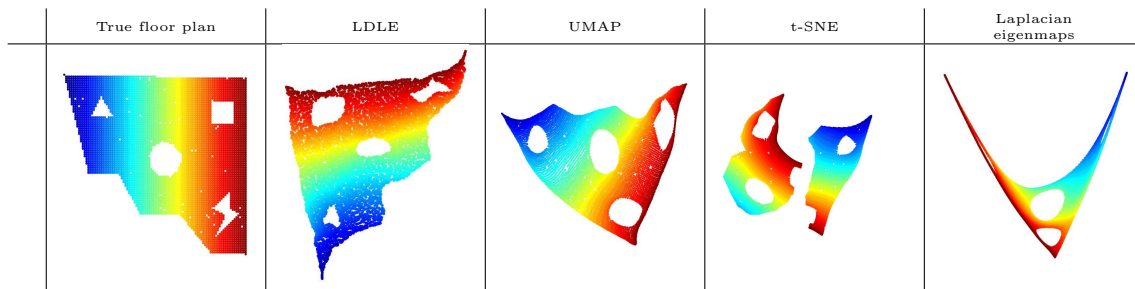


Figure 21: Embedding of the 42 dimensional signal strength data set into  $\mathbb{R}^2$  (see Section 6.3 for details).

## References

- [1] S. T. Roweis, L. K. Saul, Nonlinear dimensionality reduction by locally linear embedding, *science* 290 (5500) (2000) 2323–2326.
- [2] D. L. Donoho, C. Grimes, Hessian eigenmaps: Locally linear embedding techniques for high-dimensional data, *Proceedings of the National Academy of Sciences* 100 (10) (2003) 5591–5596.
- [3] M. Belkin, P. Niyogi, Laplacian eigenmaps for dimensionality reduction and data representation, *Neural computation* 15 (6) (2003) 1373–1396.
- [4] L. v. d. Maaten, G. Hinton, Visualizing data using t-SNE, *Journal of machine learning research* 9 (Nov) (2008) 2579–2605.
- [5] L. McInnes, J. Healy, J. Melville, Umap: Uniform manifold approximation and projection for dimension reduction, *arXiv preprint arXiv:1802.03426*.
- [6] P. W. Jones, M. Maggioni, R. Schul, Universal local parametrizations via heat kernels and eigenfunctions of the Laplacian, *arXiv preprint arXiv:0709.1975*.
- [7] N. Saito, How Can We Naturally Order and Organize Graph Laplacian Eigenvectors?, in: *2018 IEEE Statistical Signal Processing Workshop (SSP)*, 2018, pp. 483–487. doi:10.1109/SSP.2018.8450808.
- [8] Y.-C. Chen, M. Meila, Selecting the independent coordinates of manifolds with large aspect ratios, in: *Advances in Neural Information Processing Systems*, Vol. 32, Curran Associates, Inc., 2019, pp. 1088–1097. URL <https://proceedings.neurips.cc/paper/2019/file/6a10bbd480e4c5573d8f3af73ae0454b-Paper.pdf>
- [9] C. J. Dsilva, R. Talmon, R. R. Coifman, I. G. Kevrekidis, Parsimonious representation of nonlinear dynamical systems through manifold learning: A chemotaxis case study, *Applied and Computational Harmonic Analysis* 44 (3) (2018) 759 – 773. doi:<https://doi.org/10.1016/j.acha.2015.06.008>. URL <http://kkk.sciencedirect.com/science/article/pii/S1063520315000949>
- [10] Y. Blau, T. Michaeli, Non-Redundant Spectral Dimensionality Reduction, *CoRR* abs/1612.03412. arXiv:1612.03412. URL <http://arxiv.org/abs/1612.03412>
- [11] R. R. Coifman, S. Lafon, Diffusion maps, *Applied and computational harmonic analysis* 21 (1) (2006) 5–30.
- [12] S. Steinerberger, On the spectral resolution of products of Laplacian eigenfunctions, *arXiv preprint arXiv:1711.09826*.
- [13] A. Cloninger, S. Steinerberger, On the Dual Geometry of Laplacian Eigenfunctions, *Experimental Mathematics* 0 (0) (2018) 1–11. arXiv:<https://doi.org/10.1080/10586458.2018.1538911>, doi:10.1080/10586458.2018.1538911. URL <https://doi.org/10.1080/10586458.2018.1538911>
- [14] D. Li, D. B. Dunson, Geodesic distance estimation with spherelets, *arXiv preprint arXiv:1907.00296*.
- [15] L. Zelnik-Manor, P. Perona, Self-tuning spectral clustering, in: *Advances in neural information processing systems*, 2005, pp. 1601–1608.
- [16] S. Lafon, *Diffusion Maps and Geometric Harmonics*, PhD Thesis (2004) 45.
- [17] F. Crosilla, A. Beinat, Use of generalised Procrustes analysis for the photogrammetric block adjustment by independent models, *ISPRS Journal of Photogrammetry and Remote Sensing* 56 (2002) 195–209. doi:10.1016/S0924-2716(02)00043-6.
- [18] J. C. Gower, Generalized procrustes analysis, *Psychometrika* 40 (1) (1975) 33–51.
- [19] J. M. Ten Berge, Orthogonal Procrustes rotation for two or more matrices, *Psychometrika* 42 (2) (1977) 267–276.
- [20] J. C. Gower, G. B. Dijkstra, et al., *Procrustes problems*, Vol. 30, Oxford University Press on Demand, 2004.
- [21] MATLAB, *Procrustes analysis*, *Statistics and Machine Learning Toolbox*, The MathWorks, Natick, MA, USA, 2018.
- [22] E. Peterfreund, O. Lindenbaum, F. Dietrich, T. Bertalan, M. Gavish, I. G. Kevrekidis, R. R. Coifman, LOCA: LOcal Conformal Autoencoder for standardized data coordinates, *arXiv preprint arXiv:2004.07234*.
- [23] A. Y. Ng, M. I. Jordan, Y. Weiss, On Spectral Clustering: Analysis and an Algorithm, in: *Proceedings of the 14th International Conference on Neural Information Processing Systems: Natural and Synthetic*, NIPS’01, MIT Press, Cambridge, MA, USA, 2001, p. 849–856.
- [24] T. Berry, T. Sauer, Density estimation on manifolds with boundary, *Computational Statistics & Data Analysis* 107 (2017) 1–17.
- [25] A. Cloninger, W. Czaja, Eigenvector localization on data-dependent graphs, in: *2015 International Conference on Sampling Theory and Applications (SampTA)*, 2015, pp. 608–612. doi:10.1109/SAMP.2015.7148963.

- [26] G. Mishne, I. Cohen, Multiscale anomaly detection using diffusion maps, *IEEE Journal of Selected Topics in Signal Processing* 7 (1) (2013) 111–123. doi:10.1109/JSTSP.2012.2232279.
- [27] X. Cheng, G. Mishne, Spectral embedding norm: Looking deep into the spectrum of the graph laplacian, *SIAM Journal on Imaging Sciences* 13 (2) (2020) 1015–1048.
- [28] G. Mishne, U. Shaham, A. Cloninger, I. Cohen, Diffusion nets, *Applied and Computational Harmonic Analysis* 47 (2) (2019) 259 – 285. doi:https://doi.org/10.1016/j.acha.2017.08.007.
- [29] G. Mishne, R. R. Coifman, M. Lavzin, J. Schiller, Automated cellular structure extraction in biological images with applications to calcium imaging data, *bioRxiv*doi:10.1101/313981.
- [30] Y. Canzani, Analysis on manifolds via the Laplacian.
- [31] P. H. Schönemann, A generalized solution of the orthogonal procrustes problem, *Psychometrika* 31 (1) (1966) 1–10.

## Appendix A. Proof of Theorem 2

Choose  $\epsilon > 0$  so that the exponential map  $\exp_x : T_x\mathcal{M} \rightarrow \mathcal{M}$  is a well defined diffeomorphism on  $\mathcal{B}_{2\epsilon} \subset T_x\mathcal{M}$  where  $T_x\mathcal{M}$  is the tangent space to  $\mathcal{M}$  at  $x$ ,  $\exp_x(0) = x$  and

$$\mathcal{B}_\epsilon = \{v \in T_x\mathcal{M} \mid \|v\|_2 < \epsilon\}. \quad (\text{A.1})$$

Then using [30, lem. 48, prop. 50, th. 51], for all  $y \in B_\epsilon(x)$  such that

$$B_\epsilon(x) = \{y \in \mathcal{M} \mid d_g(x, y) < \epsilon\} \quad (\text{A.2})$$

we have,

$$p(t, x, y) = G(t, x, y)(u_0(x, y) + tu_1(x, y) + O(t^2)), \quad (\text{A.3})$$

where

$$G(t, x, y) = \frac{e^{-d_g(x, y)^2/4t}}{(4\pi t)^{d/2}}, \quad (\text{A.4})$$

$$u_0(x, y) = 1 + O(\|v\|^2), \quad y = \exp_x(v), v \in T_x\mathcal{M}, \quad (\text{A.5})$$

and for  $f \in C(\mathcal{M})$ , the following hold

$$f(x) = \lim_{t \rightarrow 0} \int_{\mathcal{M}} p(t, x, y) f(y) \omega_g(y) \quad (\text{A.6})$$

$$= \lim_{t \rightarrow 0} \int_{B_\epsilon(x)} p(t, x, y) f(y) \omega_g(y), \quad (\text{A.7})$$

$$f(x) = \lim_{t \rightarrow 0} \int_{B_\epsilon(x)} G(t, x, y) f(y) \omega_g(y), \quad (\text{A.8})$$

$$u_1(x, x) f(x) = \lim_{t \rightarrow 0} \int_{B_\epsilon(x)} G(t, x, y) u_1(x, y) f(y) \omega_g(y). \quad (\text{A.9})$$

Using the above equations and the definition of  $\Psi_{kij}(y)$  in Eq. (12) and  $A_{kij}$  in Eq. (13) we compute the limiting value of the scaled local correlation (see Eq. (16)),

$$\tilde{A}_{kij} = \lim_{t \rightarrow 0} \frac{A_{kij}}{2t} \quad (\text{A.10})$$

$$= \lim_{t \rightarrow 0} \frac{1}{2t} \int_{\mathcal{M}} p(t, x_k, y) \Psi_{kij}(y) \omega_g(y). \quad (\text{A.11})$$

which will turn out to be the inner product between the gradients of the eigenfunctions  $\phi_i$  and  $\phi_j$  at  $x_k$ . We start by choosing an  $\epsilon_k > 0$  so that  $\exp_{x_k}$  is a well defined diffeomorphism on  $\mathcal{B}_{2\epsilon_k} \subset T_{x_k}\mathcal{M}$ . Using Eq. (A.7) we change the region of integration from  $\mathcal{M}$  to  $B_{\epsilon_k}(x_k)$ ,

$$\tilde{A}_{kij} = \lim_{t_k \rightarrow 0} \frac{1}{2t_k} \int_{B_{\epsilon_k}(x_k)} p(t_k, x_k, y) \Psi_{kij}(y) \omega_g(y). \quad (\text{A.12})$$

Substitute  $p(t_k, x_k, y)$  from Eq. (A.3) and simplify using Eq. (A.8, A.9) and the fact that  $\Psi_{kij}(x_k) = 0$  to get

$$\begin{aligned}
\tilde{A}_{kij} &= \lim_{t_k \rightarrow 0} \frac{1}{2t_k} \int_{B_{\epsilon_k}(x_k)} G(t_k, x_k, y) (u_0(x_k, y) + t_k u_1(x_k, y) + O(t_k^2)) \Psi_{kij}(y) \omega_g(y). \\
&= \lim_{t_k \rightarrow 0} \left( \frac{1}{2t_k} \int_{B_{\epsilon_k}(x_k)} G(t_k, x_k, y) u_0(x_k, y) \Psi_{kij}(y) \omega_g(y) + \right. \\
&\quad \left. \frac{t_k u_1(x_k, x_k) \Psi_{kij}(x_k) + O(t_k^2) \Psi_{kij}(x_k)}{2t_k} \right) \\
&= \lim_{t_k \rightarrow 0} \frac{1}{2t_k} \int_{B_{\epsilon_k}(x_k)} G(t_k, x_k, y) u_0(x_k, y) \Psi_{kij}(y) \omega_g(y). \tag{A.13}
\end{aligned}$$

Replace  $y \in B_{\epsilon_k}(x_k)$  by  $\exp_{x_k}(v)$  where  $v \in \mathcal{B}_{\epsilon_k} \subset T_{x_k} \mathcal{M}$  and  $\|v\| = d_g(x_k, y)$ . Denote the Jacobian for the change of variable by  $J(v)$  i.e.  $J(v) = \frac{d}{dv} \exp_{x_k}(v)$ . Note that  $\exp_{x_k}(0) = x_k$  and  $J(0) = I$ . Using the Taylor expansion of  $\phi_i$  and  $\phi_j$  about 0 we obtain

$$\begin{aligned}
\phi_s(y) &= \phi_s(\exp_{x_k}(v)) = \phi_s(\exp_{x_k}(0)) + \nabla \phi_s(\exp_{x_k}(0))^T J(0)v + O(\|v\|^2) \\
&= \phi_s(x_k) + \nabla \phi_s(x_k)^T v + O(\|v\|^2), \quad s = i, j. \tag{A.14}
\end{aligned}$$

Substituting the above equation in the definition of  $\Psi_{kij}(y)$  (see Eq. (12)) we get

$$\begin{aligned}
\Psi_{kij}(y) &= \Psi_{kij}(\exp_{x_k}(v)) \\
&= v^T \nabla \phi_i \nabla \phi_j^T v + (\nabla \phi_i^T v + \nabla \phi_j^T v) O(\|v\|^2) + O(\|v\|^4), \tag{A.15}
\end{aligned}$$

where  $\nabla \phi_s \equiv \nabla \phi_s(x_k)$ ,  $s = i, j$ . Now we substitute Eq. (A.15, A.4, A.5) in Eq. (A.13) while replacing variable  $y$  with  $\exp_{x_k}(v)$  where  $J(v)$  is the Jacobian for the change of variable as before, to get

$$\begin{aligned}
\tilde{A}_{kij} &= \lim_{t_k \rightarrow 0} \frac{1}{2t_k} \int_{\mathcal{B}_{\epsilon_k}} \frac{e^{-\|v\|^2/4t_k}}{(4\pi t_k)^{d/2}} (1 + O(\|v\|^2)) \Psi_{kij}(\exp_{x_k}(v)) J(v) dv \\
&= L_1 + L_2, \tag{A.16}
\end{aligned}$$

where  $L_1$  and  $L_2$  are the terms obtained by expanding  $1 + O(\|v\|^2)$  in the integrand. We will show that  $L_2 = 0$  and  $\tilde{A}_{kij} = L_1 = \nabla \phi_i^T \nabla \phi_j$ .

$$\begin{aligned}
L_2 &= \lim_{t_k \rightarrow 0} \frac{1}{2t_k} \int_{\mathcal{B}_{\epsilon_k}} \frac{e^{-\|v\|^2/4t_k}}{(4\pi t_k)^{d/2}} O(\|v\|^2) (\text{tr}(\nabla \phi_i \nabla \phi_j^T v v^T) + \\
&\quad (\nabla \phi_i^T v + \nabla \phi_j^T v) O(\|v\|^2) + O(\|v\|^4)) J(v) dv \\
&= \lim_{t_k \rightarrow 0} \frac{1}{2t_k} (O(t_k^2) + 0 + 0 + O(t_k^4)) \\
&= 0. \tag{A.17}
\end{aligned}$$



Therefore,

$$\begin{aligned}\tilde{A}_{kij} &= L_1 \\ &= \lim_{t_k \rightarrow 0} \frac{1}{2t_k} \int_{\mathcal{B}_{\epsilon_k}} \frac{e^{-\|v\|^2/4t_k}}{(4\pi t_k)^{d/2}} \Psi_{kij}(\exp_{x_k}(v)) J(v) dv\end{aligned}\tag{A.18}$$

$$\begin{aligned}&= \lim_{t_k \rightarrow 0} \frac{1}{2t_k} \int_{\mathcal{B}_{\epsilon_k}} \frac{e^{-\|v\|^2/4t_k}}{(4\pi t_k)^{d/2}} (v^T \nabla \phi_i \nabla \phi_j^T v + \\ &\quad (\nabla \phi_i^T v + \nabla \phi_j^T v) O(\|v\|^2) + O(\|v\|^4)) J(v) dv \\ &= \lim_{t_k \rightarrow 0} \frac{1}{2t_k} \int_{\mathcal{B}_{\epsilon_k}} \frac{e^{-\|v\|^2/4t_k}}{(4\pi t_k)^{d/2}} v^T \nabla \phi_i \nabla \phi_j^T v J(v) dv + \frac{0 + 0 + O(t_k^2)}{2t_k} \\ &= \lim_{t_k \rightarrow 0} \frac{1}{2t_k} \int_{\mathcal{B}_{\epsilon_k}} \frac{e^{-\|v\|^2/4t_k}}{(4\pi t_k)^{d/2}} v^T \nabla \phi_i \nabla \phi_j^T v J(v) dv.\end{aligned}\tag{A.19}$$

Substitution of  $t_k = 0$  leads to the indeterminate form  $\frac{0}{0}$ . Therefore, we apply L'Hospital's rule and then Leibniz integral rule to get,

$$\begin{aligned}\tilde{A}_{kij} &= \lim_{t_k \rightarrow 0} \frac{1}{2} \int_{\mathcal{B}_{\epsilon_k}} \left( \frac{\|v\|^2}{4t_k^2} - \frac{d}{2t_k} \right) \frac{e^{-\|v\|^2/4t_k}}{(4\pi t_k)^{d/2}} v^T \nabla \phi_i \nabla \phi_j^T v J(v) dv \\ &= \text{tr} \left( \frac{1}{2} \nabla \phi_i \nabla \phi_j^T \lim_{t_k \rightarrow 0} \int_{\mathcal{B}_{\epsilon_k}} \left( \frac{\|v\|^2}{4t_k^2} - \frac{d}{2t_k} \right) \frac{e^{-\|v\|^2/4t_k}}{(4\pi t_k)^{d/2}} v v^T J(v) dv \right) \\ &= \text{tr} \left( \frac{1}{2} \nabla \phi_i \nabla \phi_j^T \left( \lim_{t_k \rightarrow 0} \left( \frac{(12 + 4(d-1))t_k^2}{4t_k^2} - \frac{2t_k d}{2t_k} \right) I + O(t_k) I \right) \right) \\ &= \nabla \phi_i^T \nabla \phi_j.\end{aligned}\tag{A.20}$$

Finally, note that the Eq. (A.18) is same as the following equation with  $y$  replaced by  $\exp_{x_k}(v)$ ,

$$\tilde{A}_{kij} = \lim_{t_k \rightarrow 0} \frac{1}{2t_k} \int_{B_{\epsilon_k}(x_k)} G(t_k, x_k, y) \Psi_{kij}(y) \omega_g(y).\tag{A.21}$$

We used the above equation to estimate  $\tilde{A}_{kij}$  in Section 3.1. □

## Appendix B. Rationale behind the choice of $t_k$ in Eq. (20)

Since  $|\mathcal{M}| \leq 1$ , we note that

$$\epsilon_k \leq \Gamma(d/2 + 1)^{1/d} / \sqrt{\pi}\tag{B.1}$$

where the maximum can be achieved when  $\mathcal{M}$  is a  $d$ -dimensional ball of unit volume. Then we take the limiting value of  $t_k$  as in Eq. (20) where  $\text{chi2inv}$  is the inverse cdf of the chi-squared distribution with  $d$  degrees of freedom evaluated at  $p$ . Since the covariance matrix of  $G(t_k, x, y)$  is  $\sqrt{2t_k}I$  (see Eq. (18)), the above value of  $t_k$  ensures  $p$  probability mass to lie in  $B_{\epsilon_k}(x_k)$ . We take  $p$  to be 0.99 in our experiments. Also, using Eq. (B.1) and Eq. (20) we have

$$t_k \leq \frac{1}{2\pi} \frac{\Gamma(d/2 + 1)^{2/d}}{\text{chi2inv}(p, d)} \ll 1, \text{ when } p = 0.99.\tag{B.2}$$

Using the above inequality with  $p = 0.99$ , for  $d = 2, 10, 100$  and  $1000$ , the upper bound on  $t_k = 0.0172, 0.018, 0.0228$  and  $0.0268$  respectively. Thus,  $t_k$  is indeed a small value close to 0.



### Appendix C. Construction of $\mathcal{S}$ in Algo. 4

In Algo. 4, the set  $\mathcal{S}$  contained the indices of the points for which the cost of moving and the destination clusters are recomputed at the end of an iteration. These indices correspond to the points which belong to the cluster  $d_k$  or has  $d_k$  as the destination cluster or has  $s$  as the neighboring cluster. We now provide the reason for recomputing the cost of moving for the points with these indices.

**Case 1.** After moving  $x_k$  to  $d_k$ , if  $|\mathcal{C}_{d_k}|$  becomes greater than  $\eta$ , then the cluster  $d_k$  was not small prior to the move. Therefore,  $x_k$  will not be moved anymore and we must update  $\text{cost}_k$  to infinity. If  $|\mathcal{C}_{d_k}|$  becomes  $\eta$  then the cluster  $d_k$  was small prior to the move but it is not small anymore. Therefore, we need to update the cost of all the points in cluster  $d_k$  to be infinity as none of these points will be moved anymore. If  $|\mathcal{C}_{d_k}|$  is less than  $\eta$  then the cluster  $d_k$  is still small. So  $x_k$  may be moved again and therefore its destination cluster and cost of moving must be updated. Therefore, the cost of moving is updated for all the points in cluster  $d_k$ .

**Case 2.** Suppose  $x_j$  is a point in a small cluster whose destination cluster is  $d_k$ , that is  $d_j = d_k$ . Prior to moving  $x_k$  to  $d_k$  the cost of moving  $x_j$  to  $d_k$  was  $\text{Distortion}(\tilde{\Phi}_{d_k}, U_j \cup \tilde{U}_{d_k})$  (see Eq. (44)). After moving  $x_k$  to cluster  $d_k$ , the neighbors of the cluster  $d_k$  will expand to  $\tilde{U}_{d_k} \cup U_k$ . Then, the new cost of moving  $x_j$  to  $d_k$  is  $\text{Distortion}(\tilde{\Phi}_{d_k}, U_j \cup \tilde{U}_{d_k} \cup U_k)$ . Therefore, the the cost of moving all the points whose destination cluster is  $d_k$  must be updated.

**Case 3.** Suppose after moving  $x_k$  out of cluster  $s$  it becomes empty. Since  $|\mathcal{C}_s| = 0$ , the cost of moving any other point to cluster  $s$  is infinity as the third condition in Eq. (44) no longer holds. Therefore, we must recompute the cost of moving all those points whose destination cluster is cluster  $s$ . These points form a subset of the points which have cluster  $s$  as the neighboring cluster.

**Case 4.** Suppose after moving  $x_k$  out of cluster  $s$  it is still non-empty. Also, suppose that  $x_j$  is a point in a small cluster with cluster  $s$  as its neighboring cluster. This means  $s \in c_{U_j}$ . Prior to moving  $x_k$  out of cluster  $s$  the cost of moving  $x_j$  to cluster  $s$  was  $\text{Distortion}(\tilde{\Phi}_s, I_j \cup \tilde{U}_s)$  (see Eq. (44)). After moving  $x_k$  out of cluster  $s$ ,  $\tilde{U}_s$  will possibly contract (see Eq. (42)). Therefore, the cost of moving all the points with cluster  $s$  as a neighboring cluster must be updated.

### Appendix D. Computation of $(s_m, p_m)_{m=1}^M$ in Algo. 5

Algo. 5 aligns the intermediate views in a sequence. The computation of these sequences is motivated by the necessary and sufficient conditions for a unique solution to the standard orthogonal Procrustes problem. We start by a brief review of a variant of the orthogonal Procrustes problem. Given the two matrices  $A$  and  $B$  of same size with  $d$  columns, one asks for an orthogonal matrix  $T$  of size  $d \times d$  and a  $d$ -dimensional columns vector  $v$  which most closely map  $A$  to  $B$ , that is,

$$T, v = \underset{\Omega, \omega}{\text{argmin}} \|A\Omega + \mathbf{1}_n \omega^T - B\|_F^2 \quad \text{such that } \Omega^T \Omega = I. \quad (\text{D.1})$$

Here  $\mathbf{1}_n$  is the  $n$ -dimensional column vector containing ones. Equating the derivative of the objective with respect to  $\omega$  to zero, we obtain the following condition for  $\omega$ ,

$$\omega = \frac{\mathbf{1}_n^T}{n} (A\Omega - B). \quad (\text{D.2})$$

Substituting this back in Eq. (D.1), we reduce the above problem to the standard orthogonal Procrustes problem,

$$T = \underset{\Omega}{\text{argmin}} \|\bar{A}\Omega - \bar{B}\|_F^2 \quad (\text{D.3})$$

where

$$\bar{X} = \left( I - \frac{1}{n} \mathbf{1}_n \mathbf{1}_n^T \right) X \quad (\text{D.4})$$

for any matrix  $X$ . This is equivalent to subtracting the mean of the rows in  $X$  from each row of  $X$ .

As proved in [31], the above problem, and therefore the variant, has a unique solution if and only if the square matrix  $\bar{A}^T \bar{B}$  has full rank  $d$ . Denote by  $\sigma_d(X)$  the  $d$ th smallest singular value of  $X$ . Then  $\bar{A}^T \bar{B}$  has full rank if  $\sigma_d(\bar{A}^T \bar{B})$  is non-zero, otherwise there exists multiple  $T$  which minimize Eq. (D.1).

Now, we come back to the computation of the sequences  $(s_m, p_m)_{m=1}^M$ . The first view in the sequence corresponds to the largest cluster,

$$s_1 = \operatorname{argmax}_m |\mathcal{C}_m|. \quad (\text{D.5})$$

For convenience, we denote  $s_m$  by  $s$ ,  $p_m$  by  $p$  and  $V_{mm'}$  by  $\tilde{\Phi}_m^g(\tilde{U}_{mm'})$  whenever needed. Then the sequences  $(s_m)_{m=2}^M$  and  $(p_m)_{m=2}^M$  are computed so that  $(T_s, v_s)$  can be estimated without any *ambiguity*, to align the view  $\tilde{\Phi}_s^g(\tilde{U}_{sp})$  with the view  $\tilde{\Phi}_p^g(\tilde{U}_{sp})$ . The alignment is done by minimizing the objective in Eq. D.1 with  $A$  and  $B$  replaced by  $V_{sp}$  and  $V_{ps}$ . An ambiguity would arise if multiple values of  $(T_s, v_s)$  can align the two views. This happens when  $\sigma_d(\bar{V}_{sp}^T \bar{V}_{ps})$  is zero.

We therefore quantify the ambiguity in aligning the  $m$ th and the  $m'$ th intermediate views on their overlap, that is,  $V_{mm'}$  and  $V_{m'm}$ , by

$$W_{mm'} = \sigma_d(\bar{V}_{mm'}^T \bar{V}_{m'm}). \quad (\text{D.6})$$

Note that  $W_{mm'} = W_{m'm}$ . Finally, we compute the sequences  $(s_m)_{m=2}^M$  and  $(p_m)_{m=2}^M$  so that  $W_{s_m p_m}$  is high for all  $m$ . To achieve this, we obtain a maximum spanning tree  $T$  rooted at  $s_1$ , of the graph with  $M$  nodes and  $W$  as the adjacency matrix (if the graph is disconnected then either  $k$  or  $\eta_{min}$  should be increased). Denote the parent of node  $k$  in  $T$  by  $\rho_k$ . Then  $(s_m)_{m=2}^M$  is the sequence in which a breadth first search visits nodes in  $T$  starting from  $s_1$ . And,  $p_m$  is the parent of  $s_m$  in the tree. Thus,

$$(s_m)_{m=2}^M = \text{Breadth-First-Search}(T, s_1) \text{ and } p_m = \rho_{s_m}. \quad (\text{D.7})$$

## Appendix E. Computation of $\tilde{U}_m^g$ in Eq. (53)

For each transformed intermediate view  $\tilde{\Phi}_m^g(\tilde{U}_m)$  in the embedding space, we first construct a secondary view  $\tilde{U}_m^g$  in the same manner as an intermediate view  $\tilde{U}_m$  in the ambient space is constructed. Then, just like Eq. (48), we define the overlap of the  $m$ th and the  $m'$ th intermediate views in the embedding space as the overlap of their secondary counterparts, given by,

$$\tilde{U}_{mm'}^g = \tilde{U}_m^g \cap \tilde{U}_{m'}^g. \quad (\text{E.1})$$

To construct  $\tilde{U}_m^g$ , we first define the discrete balls in the embedding space in the same way as in ambient space (see Eq. (21)), as

$$U_k^g = \{y_{k'} \mid d_e(y_k, y_{k'}) < \epsilon_k^g\} \quad (\text{E.2})$$

where  $\epsilon_k^g$  is the distance to the  $\nu k$ th nearest neighbor of  $y_k$ . Here, the hyperparameter  $\nu \geq 1$  scales  $k$  to account for a possibly increased separation between the points in the embedding space than in the ambient space, due to the distortion of the parameterizations  $\tilde{\Phi}_m^g$ .

Then we define the clusters in the embedding space using the same cluster labels  $c_k$  as in the ambient space, that is, the embedding  $y_k$  of  $x_k$  also belongs to cluster  $c_k$ . Now, just as  $\tilde{U}_m$  were constructed in Eq. (42), we construct  $\tilde{U}_m^g$  as

$$\tilde{U}_m^g = \cup_{c_k=m} U_k^g. \quad (\text{E.3})$$

## Appendix F. Supplementary Tables and Figures

Input Algorithm	Hyperparameters	Rectangle	Barbell	Square with two holes	Sphere with a hole	Swissroll with a hole	Noisy swissroll	Sphere	Curved torus	Flat torus	Möbius strip	Klein Bottle	42-dim signal strength data
LDLE	$\eta_{\min}$	5	5	10	5	20	15	5	18	10	10	5	5
UMAP	n_neighbors	200	200	200	200	200	200	200	200	200	200	200	50
	min_dist	0.1	0.05	0.5	0.5	0.25	0.05	0.5	0.25	0.5	0.05	0.5	0.25
t-SNE	perplexity	50	40	50	50	50	60	60	60	60	60	50	60
	exaggeration	4	6	6	4	4	4	4	4	6	4	6	4
Laplacian Eigenmaps	$k_{\text{nn}}$	-	-	16	-	-	-	-	-	-	-	-	16
	$k_{\text{tune}}$	-	-	7	-	-	-	-	-	-	-	-	7

Table F.1: The values of the hyperparameters for all the algorithms and examples. For Laplacian eigenmaps, for all the examples except square with two holes, all the searched values of the hyperparameters result in similar plots.

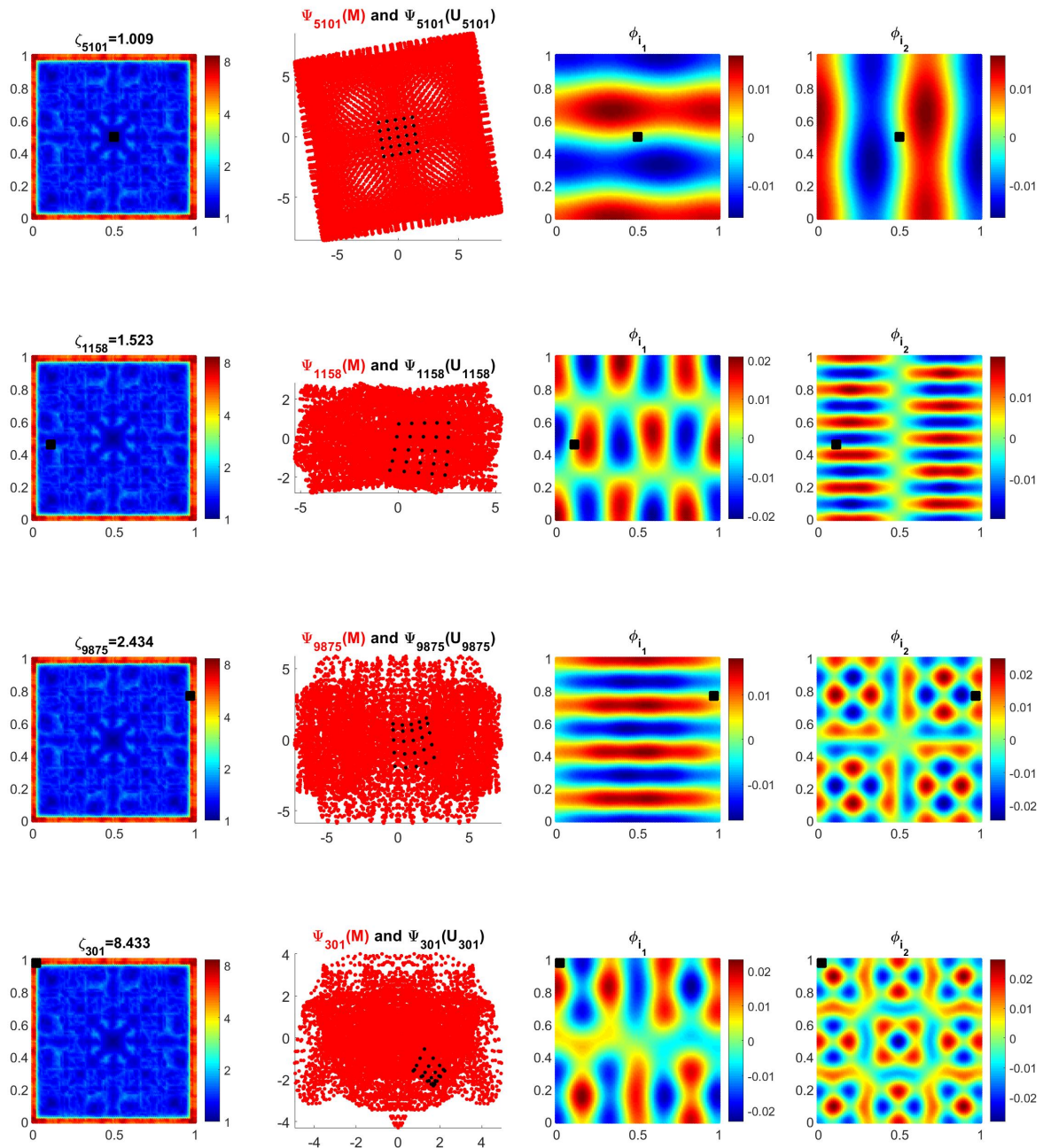


Figure F.22: (first column) Input square grid where the points are colored by the distortion of the obtained parameterizations on the neighborhood surrounding them. A local view  $U_k$  is also shown in black. (second column) The mapped square  $\Psi_k(M)$  is shown in red and the local view in the embedding space  $\Psi_k(U_k)$  is shown in black. (third column) The first eigenvector  $\phi_{ki_1}$  is shown where  $U_k$  is colored in black. (fourth column) The second eigenvector  $\phi_{ki_2}$  is shown where  $U_k$  is colored in black. Note that  $\phi_{ki_1}$  and  $\phi_{ki_2}$  are close to being orthogonal at  $x_k$ .

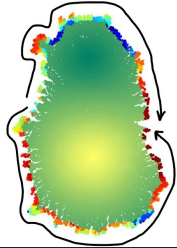
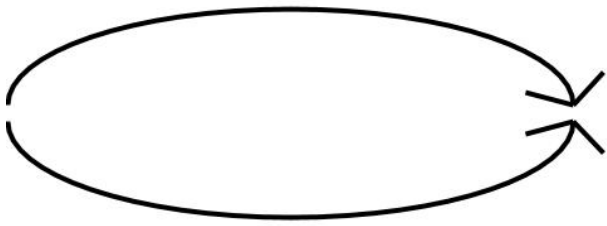
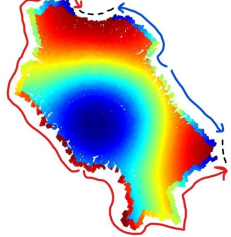
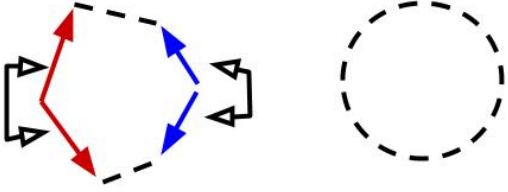
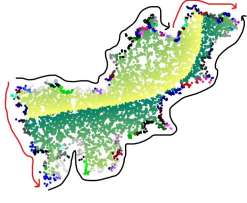

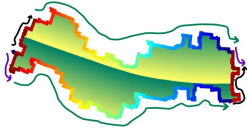
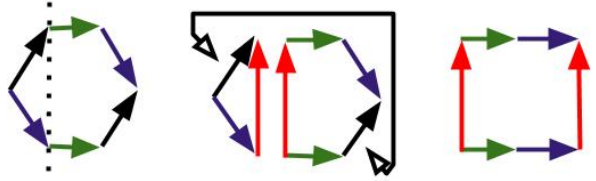
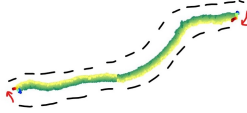


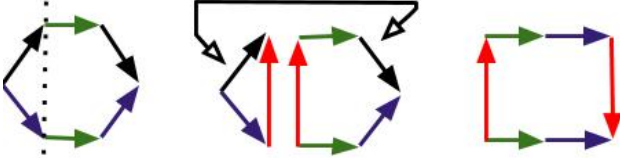
	LDLE with arrows	Derived cut and paste diagrams
Sphere		
Sphere with a hole		
Curved torus		
Flat torus		
Möbius strip		
Klein bottle		

Figure F.23: (Left) LDLE embedding with arrows drawn by tracing the colored boundary. (Right) Derived cut and paste diagrams to prove the correctness of the embedding. Filled arrows represent pieces of the boundary which are to be stitched along the arrows of the same color. Pieces of the boundary represented by dashed lines are not to be stitched. Dotted lines and shallow arrows represent cut and paste instructions.